



**Gravitational collapse of colloidal gels: Non-equilibrium phase separation driven by osmotic pressure**

Journal:	<i>Soft Matter</i>
Manuscript ID	SM-ART-01-2018-000002.R1
Article Type:	Paper
Date Submitted by the Author:	21-Feb-2018
Complete List of Authors:	Padmanabhan, Poornima; Cornell University, Chemical and Biomolecular Engineering Zia, Roseanna; Stanford University, Chemical Engineering; Chemical Engineering

Cite this: DOI: 10.1039/xxxxxxxxxx

# Gravitational collapse of colloidal gels: Non-equilibrium phase separation driven by osmotic pressure<sup>†</sup>

Poornima Padmanabhan<sup>a</sup> and Roseanna Zia<sup>b</sup>

Received Date

Accepted Date

DOI: 10.1039/xxxxxxxxxx

www.rsc.org/journalname

Delayed gravitational collapse of colloidal gels is characterized by initially slow compaction that gives way to rapid bulk collapse, posing interesting questions about the underlying mechanistic origins. Here we study gel collapse utilizing large-scale dynamic simulation of a freely draining gel of physically bonded particles subjected to gravitational forcing. The hallmark regimes of collapse are recovered: slow compaction, transition to rapid collapse, and long-time densification. Microstructural changes are monitored by tracking particle positions, coordination number, and bond dynamics, along with volume fraction, osmotic pressure, and potential energy. Together these reveal the surprising result that collapse can occur with a fully intact network, where the tipping point arises when particle migration dissolves strands in a capillary-type instability. While it is possible for collapse to rupture a gel network into clusters that then sediment, and hydrodynamic interactions can make interesting contributions, neither is necessary. Rather, we find that the “delay” arises from gravity-enhanced coarsening, which triggers the re-emergence of phase separation. The mechanism of this transition is a leap toward lower potential energy of the gel, driven by bulk negative osmotic pressure that condenses the particle phase: the gel collapses in on itself under negative osmotic pressure allowing the gel, to tunnel through the equilibrium phase diagram to a higher volume fraction “state”. Remarkably, collapse stops when condensation stops, when gravitational advection produces a positive osmotic pressure, re-arresting the gel.

## 1 Introduction

Rapid and reversible transitions between solid-like and liquid-like behavior in colloidal gels and other complex fluids underlie their extraordinary utility as engineered materials. Such transitions can be induced thermodynamically, kinetically, and mechanically in applications as diverse as injectable pharmaceuticals, drilling fluids, and flexible body armor. These “on-demand” macroscopic transitions arise from the multiphase structure of the material: microscopically small particles or chains suspended in a continuum fluid form a microstructure that deforms and relaxes relative to the fluid, over observable time scales. Bulk material deformation, phase separation, and other transformations are triggered (or resisted) at the microscopic scale by entropic, hydrodynamic, and other interactive forces that control particle rearrangements

that ultimately cascade upward to the macroscopic length scale.

Colloidal gels form a particularly important class of complex fluids, owing to their ability to simultaneously capture all three mechanisms of phase transition: the thermodynamic and kinetic phase transition that arrests to form the gel; and, as shown in our recent work, mechanical yield, flow, and re-solidification that strongly suggest non-equilibrium phase transitions.<sup>1</sup>

Hard-sphere colloids serve as an excellent model system for illustrating all aspects of thermodynamic, kinetic, and mechanical phase transitions. Distinct phases in a colloidal phase diagram (cf Figure 1) can be sampled by moving “left to right” (increasing colloid concentration) or “up and down” (strengthening interparticle attractions). In either case, the strength of particle diffusion is key to the ultimate fate of the material; weakening it via interparticle attractions or steric hindrance promotes condensation and phase separation, but such transitions are sensitively path dependent. For example, inducing interparticle attractions of order several  $kT$  (where  $k$  is Boltzmann’s constant and  $T$  is the absolute temperature) can both trigger the onset of phase separation but also arrest it, leading to formation of a bi-continuous network of condensed, glassy strands embedded

<sup>a</sup> Robert Frederick Smith School of Chemical and Biomolecular Engineering, Cornell University, Ithaca, NY, USA.

<sup>b</sup> Chemical Engineering, Stanford University, Stanford, CA, USA. E-mail: rzia@stanford.edu

<sup>†</sup> Electronic Supplementary Information (ESI) available: [details of any supplementary information available should be included here]. See DOI: 10.1039/b000000x/

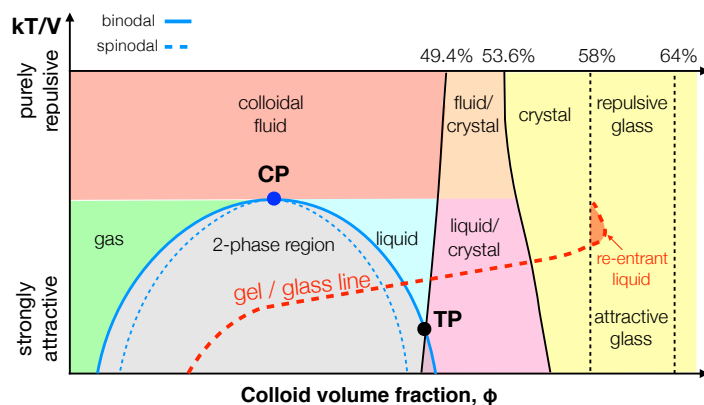


**Fig. 1** Schematic picture of equilibrium phase behavior in colloidal system with interparticle potential  $V$  and colloid volume fraction  $\phi$ . A second axis in the region  $V/kT \gg 1$  shows approximate values of  $\phi$  where transitions occur in systems of purely repulsive hard spheres.<sup>2–4</sup>

in a dilute solvent – a colloidal gel.<sup>2–7</sup> Thermal fluctuations are strong enough to rupture interparticle bonds, permitting particles on the surface of the network to migrate along strands, attracted to energetically favorable morphology.<sup>8</sup> Ongoing age-coarsening thus ratchets particles into more deeply bonded states, simultaneously seeking complete phase separation and deepening the arrest that bars it. The linear-response rheology of such gels is elastic over all frequencies and they stiffen with age.<sup>8</sup> However, they can fluidize if subjected to sufficiently strong shear.<sup>1,9–14</sup> Zia and coworkers showed that particle rearrangements and microscopic bond dynamics that permit yield under shear are consistent with a release from kinetic arrest,<sup>1,9,10</sup> and that ongoing deformation can also produce re-solidification, itself suggestive of re-arrest. A non-equilibrium phase diagram thus translates the mechanical behavior of delayed shear yield to non-equilibrium phase behavior, which we shall refer to as “phase mechanics”.

Delayed gravitational yield has been described as sudden, inexplicable collapse — owing to an initial period after gelation where the network supports its own weight but that abruptly ends with a sometimes quite rapid macroscopic collapse. The result is a dense, structureless sediment at the bottom of a container, an obviously bad outcome if one had hopes of creating a durably suspended network. On the bright side, this behavior is a clarion signal pointing to the trifecta of colloidal gel responsiveness: thermodynamic, kinetic, and mechanical phase transition.

Three macroscopic deformation regimes typify gel collapse.<sup>15–27</sup> Soon after the gel has formed, it undergoes a relatively slow reduction in macroscopic height, an “induction period” that abruptly gives way to a fast-sedimentation regime — gel collapse — during which as much as 70% of the original height is lost.<sup>22</sup> At long times, the sedimentation rate again decreases, ending with long-time compaction.<sup>19,23</sup> Early studies of this phenomenology focused primarily on understanding and developing predictive models for the connection between interparticle bond strength, particle density (weight), and particle concentration (volume fraction) to the “delay time” – the length of the time separating gel formation and the onset of rapid collapse. Visual inspection has suggested diverse structural changes during

collapse ranging from the appearance of “volcanoes” near the detaching surface,<sup>27</sup> channels and streamers in the bulk,<sup>16,17</sup> and breakup of network into clusters.<sup>15,22,26,28</sup> Approaches to formulating such models are diverse, but can be classified broadly into one of two perspectives.

In the first broad view, gel collapse is a consequence of evolving boundary conditions of the gel with its container. The attractive potential that promotes gelation (produced by e.g. non-adsorbing polymer depletant or adhering polymer bridging chains) attaches the particles to the surrounding container surfaces.<sup>29</sup> Side walls and a container bottom exert reaction forces that, along with buoyant forces, support the gel against gravitational forces.<sup>18,30</sup> A container ceiling can also permit attachment of the gel, counteracting to some extent the gravitational force acting on particles. If such a ceiling is slippery or deformable, for example a meniscus, particles embedded in it can slide along and deform it, permitting descent of the gel, which has been identified as one mechanism underlying the slow induction period;<sup>18</sup> subsequent detachment of the gel from the meniscus is then identified as the transition point to fast collapse. The model for collapse is essentially that the gel was never strong enough to support its own weight. In this scenario, bond strength, meniscus surface tension, the container dimensions and the shape of the meniscus can be connected to the detachment (delay) time.<sup>17,18,30</sup>

An alternative viewpoint holds that collapse is correlated with bulk rheological evolution.<sup>16,19,20,22,23</sup> Because gelation typically occurs within the context of at least weak gravitational effects, one must first examine the interplay between gelation and sedimentation. This can serve as a measure of the sensitivity of network connectivity to fluid backflow, for example, an important element in understanding which happens first: network rupture, followed by sedimentation, compaction that drives e.g. backflow that ruptures the network into a sedimenting suspension, or other rheological changes. However, the role of backflow does not drive the collapse, although it can certainly affect post-transition sedimentation.

Gelation can compete with sedimentation, as pointed out by Allain *et al.*<sup>16</sup> who propose that gravitational settling outpaces the lateral migration of particles required for their aggregation into clusters; the role of gravity is thus to hinder the formation of a space-spanning network, shifting the gelation boundary compared to quiescent gelation. Gelation thence requires a higher-than-predicted volume fraction of colloids, which can be achieved when sedimentation increases local particle concentration. Allain, Cloitre, and Wafra<sup>16</sup> were the first to propose that the induction period comprises this interplay, and that a transition to fast sedimentation arises from subsequent network failure caused by fluid backflow. In such a scenario, the initial sedimentation rate depends on factors that influence the formation of the gel itself: the volume fraction of colloidal particles, and the strength of interparticle attractions. While they focused on gels formed with permanent interparticle bonds, Faers<sup>31</sup> focused on reversible interparticle bonds, i.e. gels formed via arrested phase separation. His results led him to surmise that the induction period, while still a matter of ongoing gelation, spanned the time required for spinodal decomposition to arrest, and was thus set primarily by the

strength of interparticle bonds. However, the structural origins of abrupt collapse remained an open question.

We pause here to identify that Allain *et al.*'s perspective involves convolution of sedimentation with moving “left to right” in a phase diagram, while Faers' view involves moving “up and down” in a phase diagram. Their initial insights led the way to a rich body of subsequent literature interrogating the interplay between sedimentation, reversible physical gelation, and hydrodynamic effects.

Hydrodynamic interactions in dense suspensions play an important role in sedimentation that can convolve with gelation under flow. Gel formation accompanied by initial sedimentation must produce fluid backflow due to the no-flux boundary at the bottom of the container, but such backflow is hindered by the initial structure of the gel.<sup>32,33</sup> It has been proposed that early sedimentation remains slow until subsequent structural evolution produces a cascade of changes that eventually lead to large-scale network rupture. The detailed failure mechanism proposed depends on the strength of interparticle attractions.

To wit, when attractions are so strong that Brownian motion plays no role at all, the convolution between sedimentation and gelation is absent: particle rearrangements are negligibly slow compared to the time scale of sedimentation. In such a scenario, Buscall and coworkers<sup>15,32</sup> proposed that the network breaks at the bottom, densifying there first as the weight of the gel compacts it to the floor. The theory put forth to support this view is limited to very weak deformation and thus cannot predict behavior beyond the early induction period, and thus cannot tie the onset of collapse to structural changes. At the other extreme, poroelastic theory<sup>20,23,24,34,35</sup> effectively models creeping sedimentation (with no delay), or the compression of the gels during later stages of sedimentation. No theory captures the behavior of the gel from induction period through rapid sedimentation. Studies of permanent gels that do come closer to predicting collapse, e.g. by Partridge<sup>15</sup> and Allain *et al.*<sup>16</sup>, typically attribute it to backflow that ruptures the network. Such mechanisms are limited to gels where bonds are nearly permanent. However, with no detailed observations to support it, the mechanism for network failure remains unknown.

Collapse mechanisms proposed for reversibly bonded gels include the idea that aging leads to structural and rheological changes that weaken the gel. It has been argued that fluid backflow weakens the gel by further altering structure, eventually leading to network rupture. Poon and coworkers were the first to describe this perspective as a loss of ability to “heal” ruptured bonds, allowing fluid backflow to create wide channels that further increased backflow, in turn widening the channels even further. Gopalakrishnan *et al.*<sup>21</sup> extended this idea to relate bond rupture and formation, modeled via a Kramers escape time, to macroscopic delay time, but the connection between single particle dynamics and subsequent changes in structure at network length scales beyond the transition to rapid sedimentation remained unexplained. Yet another study by Kamp and Kilfoil<sup>22</sup> measured height evolution in one container and elasticity in another, by imposing oscillatory shear. They reported that the gel loses its elastic modulus at some point before or during bulk col-

lapse, but rather than create channels of fluid backflow, the gel underwent catastrophic network disintegration into clusters via an unknown mechanism that subsequently fell rapidly. The idea that elastic rigidity is lost prior to sedimentation is intriguing – but the experiment required bulk oscillation of the gel to measure the moduli, which is sufficient to trigger earlier yield,<sup>1</sup> thus preventing reliable conclusion.

Overall, where gel collapse is viewed as a bulk phenomenon, the role of interparticle attractions is central to analysis, but the mechanism of transition in reversibly bonded gels still remains murky. While many-body hydrodynamic interactions may also play a role, we focus on the detailed evolution of bond dynamics that, even in the absence of hydrodynamic interactions, play a primary role in non-equilibrium phase transitions exhibiting delay, triggered by shear stress<sup>1</sup> and under flow startup.<sup>10</sup>

In the present study, we carry out large-scale simulation of a freely-draining colloidal gel formed by arrested phase separation subjected to gravitational forcing that, after delay, triggers collapse. We show here that collapse bears the hallmarks of a “mechanical phase transition” from an arrested phase toward a more dense structure. Surprisingly, we find that this can occur with a fully intact network structure, and we show that the gel actually collapses in on itself under the pull of negative osmotic pressure arising from interparticle attractions. Overall, we argue that gravitational forcing triggers a temporary release from kinetic arrest of the colloidal gel, allowing it to traverse (or tunnel through) the equilibrium phase diagram toward a state with higher volume fraction. This non-equilibrium trajectory manifests as a leap toward lower potential energy and is driven by bulk negative osmotic pressure that condenses particles toward higher coordination number.

The remainder of the study is organized as follows: In section 2, the model system is presented. The methodology for the dynamic simulation is described in section 3, and along with the method by which the macroscopic gel height is calculated from particle positions. Results, presented in Section 4, are divided into four parts: macroscopic behavior of the gel is characterized in Section 4.1; its connection to microscopic structure are elucidated in Section 4.2; bond dynamics are examined to provide quantitative evidence for the mechanism of transition in Section 4.3; and osmotic pressure is computed to connect collapse to bulk rheology in Section 4.4. The study is concluded with a discussion in Section 5.

## 2 Model system

We study a colloidal gel formed from a suspension of 750,000 nearly-hard Brownian spheres of mean radius  $a$  initially dispersed in an implicit Newtonian solvent of viscosity  $\eta$  and density  $\rho$ . The Reynolds number is much smaller than unity,  $Re = \rho U a / \eta \ll 1$ , owing to the small size of the particles, where  $U$  is the characteristic velocity of a particle. Inertial forces in the fluid are thus much weaker than viscous stress, and fluid motion is thus governed by the Stokes equations. Crystallization is avoided by implementing a polydisperse size distribution of five equally populated particle sizes with mean  $a$  and variance 3.5%. The particles are initially randomly distributed at a volume fraction  $\phi = 4\pi a^3 n / 3 = 20\%$ .

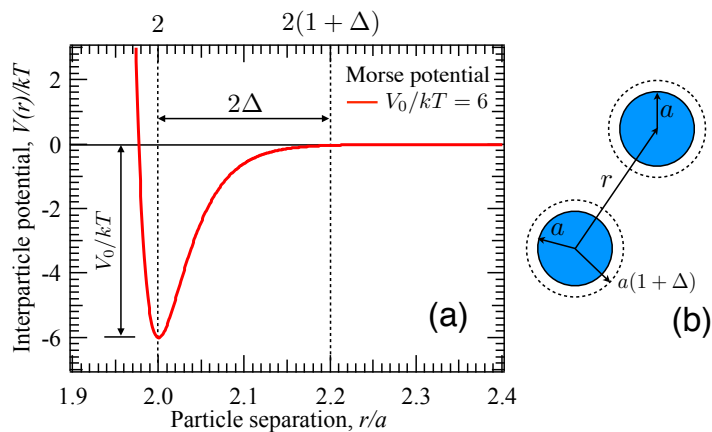


**Fig. 2** (a) Plot of the Morse potential used in the present study. (b) Colloid-depletant model system. Dashed lines enclose the volume excluded to the depletants.

Gelation follows introduction of a short-range attractive potential, as would be induced by the addition of non-adsorbing depletant molecules,<sup>36</sup> or attachment of bridging chains,<sup>37</sup> for example. A pairwise Morse potential  $V_{ij}$  provides a tunable model of such interactions:

$$V_{ij}(r_{ij}) = -V_0 \left[ 2e^{-\kappa(r_{ij} - (a_i + a_j))} - e^{-2\kappa(r_{ij} - (a_i + a_j))} \right]. \quad (1)$$

Here,  $r_{ij}$  is the distance separating particles  $i$  and  $j$  with radii  $a_i$  and  $a_j$ . The characteristic strength of attraction,  $V_0$ , is chosen such that bonds are durable but reversible,  $5kT \leq V_0 \leq 6kT$ . The range of the potential is set by  $\kappa = 30/a$  which corresponds to a depletant-to-colloid size ratio, or bridging chain average radius of gyration-to-colloid ratio<sup>37</sup>  $\Delta = 0.1$ . Hydrodynamic interactions between particles are neglected. This system was described in detail in our previous study of age coarsening and its impact on dynamics and linear-response rheology.<sup>8</sup>

The gel is replicated periodically in the  $x$  and  $y$  directions of an orthogonal reference frame, whilst no-flux boundaries are imposed at the bottom ( $z = 0$ ) and top ( $z = H$ ) of the simulation cell to model a hard, flat, and impermeable floor and ceiling. Particles are prevented from passing through the wall via a steep repulsive potential, detailed in the Supplementary Materials.

To mimic experimental studies where the sample is typically sealed in a tube and tumbled for several hours allowing the sample to gel to attach to the walls and menisci, we age the gel in the presence of walls in the absence of gravity for 100 Brownian times,  $100 a^2/D$ , where  $1 a^2/D$  is the time it takes an isolated particle to diffuse its size in solvent.

### 3 Dynamic Simulation Method

Gravity is imposed by exerting a body force on all particles, which mimics a density mismatch between colloids and solvent. Colloidal dynamics in Stokes flow are governed by the Langevin equation, where particles are acted upon by hydrodynamic, Brownian, interparticle, and buoyant forces:

$$\mathbf{m} \cdot \frac{d\mathbf{U}}{dt} = \mathbf{F}^H + \mathbf{F}^B + \mathbf{F}^P + \mathbf{F}^G. \quad (2)$$

Here,  $\mathbf{m}$  is the mass or moment of inertia tensor of the particle,  $\mathbf{U}$  is particle velocity, and  $\mathbf{F}^H$ ,  $\mathbf{F}^B$ ,  $\mathbf{F}^P$ , and  $\mathbf{F}^G$  are hydrodynamic, Brownian, interparticle, and buoyant forces respectively. The hydrodynamic force on a particle  $i$  in a freely draining suspension is given by Stokes' drag law:

$$\mathbf{F}_i^H = -6\pi\eta a_i \mathbf{U}_i, \quad (3)$$

where  $\mathbf{U}$  is the particle velocity. The stochastic Brownian force, averaged over many collisions with solvent particles, obeys Gaussian statistics with zero mean and co-variance set by the fluctuation dissipation theorem:

$$\overline{\mathbf{F}_i^B} = 0, \quad \overline{\mathbf{F}_i^B(0) \mathbf{F}_i^B(t)} = 2kT(6\pi\eta a_i) \mathbf{I} \delta(t), \quad (4)$$

where the overbar denotes an average over times long compared to the inertial relaxation of a particle. The Brownian impacts are instantaneously correlated, where  $\delta(t)$  is the Dirac delta function. The interparticle force is derivable from the spherically symmetric potential,  $\mathbf{F}^P = -\nabla V(r)$ , (cf Equation 1), and is summed over the contribution from all particles  $j$  interacting with particle  $i$  (or a nearby wall):

$$\mathbf{F}_i^P = -\sum_j \frac{\partial V_{ij}(r_{ij})}{\partial r_{ij}} \hat{\mathbf{r}}_{ij} - \frac{\partial V_{i,w}}{\partial r_{i,w}} \hat{\mathbf{r}}_{i,w}. \quad (5)$$

Here,  $\hat{\mathbf{r}}_{ij}$  is the unit vector pointing from the center of particle  $j$  to the center of particle  $i$ , and  $\hat{\mathbf{r}}_{i,w}$  is the unit vector pointing from the wall to the center of particle  $i$ . The gravitational force on each particle is given by:

$$\mathbf{F}_i^G = \frac{4\pi}{3} \Delta\rho a_i^3 \mathbf{g}, \quad (6)$$

where  $\Delta\rho$  is the density mismatch between colloids and solvent, and  $\mathbf{g}$  is the acceleration due to gravity.

The dynamic equations are integrated forward in time to obtain instantaneous particle positions and velocities using velocity Verlet integration, implemented by the LAMMPS molecular dynamics software package.<sup>38</sup> Selection of a small time step enforces Stokesian physics, the regime where both Reynolds and Stokes numbers are vanishingly small, as shown in our prior work.<sup>8</sup> In this overdamped regime of colloidal motion, inertia does not matter and thus motion is set by a balance between gravitational, Brownian, and interparticle forces. Bond durability is set by the strength of attractions relative to diffusion,  $V_0/kT$ . The strength of the gravitational force relative to the entropic force, also influences relative particle motion. We recall that gravitational settling of purely repulsive hard spheres in a container creates a concentration gradient that drives diffusive flux upward that in turn resists sedimentation, giving a natural force scaling: a gravitational Péclet number  $Pe = (4\pi/3)\Delta\rho a^3 g / (kT/a)$ , a measure of the strength of advective settling  $\Delta\rho a^3 g$  relative to entropic resistance  $kT/a$ . In the present study, values were chosen to match those studied in the experimental literature:  $0.01 \leq Pe \leq 0.1$ . Together,  $Pe$  and  $V_0/kT$  determine particle-scale motion.

Detection of collapse and measurement of subsequent sedimentation rate requires identification and tracking of an emergent free surface. In experiments, dark field imaging<sup>17</sup> is utilized to

identify the height of the gel formed by a clearly distinguishable interface between colloid-rich gel and colloid-poor supernatant. One method for finding a free interface is to distinguish between the low volume-fraction (colloid-poor) supernatant and the high volume-fraction (colloid-rich) gel. However, as the gel detaches from the container ceiling, the newly exposed surface in both experiments and simulations is quite rough, comprising exposed pores and dangling strands of highly heterogeneous volume fraction. We developed an algorithm to interrogate spatial variation in volume fraction, described in Appendix A to give an unambiguous measurement of the position of the bulk top surface of the gel.

The total stress  $\langle \boldsymbol{\sigma} \rangle$  in the gel is averaged over the entire volume and can be separated into contributions from the solvent and that due to the particles,  $\langle \boldsymbol{\Sigma} \rangle$ , following the approach of Batchelor.<sup>39,40</sup> The particle-phase stress in general includes contributions from Brownian, interparticle, and externally driven hydrodynamic forces:

$$\langle \boldsymbol{\Sigma} \rangle = -nkT\mathbf{I} + \langle \boldsymbol{\Sigma}^B \rangle + \langle \boldsymbol{\Sigma}^P \rangle + \langle \boldsymbol{\Sigma}^{H,ext} \rangle, \quad (7)$$

where the first term is the ideal osmotic pressure arising from the presence of the particles. Brownian motion contributes first to the interparticle stress  $\langle \boldsymbol{\Sigma}^P \rangle$  and, if hydrodynamic interactions are present, produces disturbance flows that create Brownian stress,  $\langle \boldsymbol{\Sigma}^B \rangle$ . In the freely draining limit, the latter vanishes, as does  $\langle \boldsymbol{\Sigma}^{H,ext} \rangle$ . The remaining interparticle stress  $n\langle \mathbf{x}\mathbf{F}^P \rangle$  includes the so-called elastic stress (entropic exclusion), as well as contributions from attractive forces:

$$\langle \boldsymbol{\Sigma} \rangle = -nkT\mathbf{I} + n\langle \mathbf{r}\mathbf{F}^P \rangle, \quad (8)$$

where  $\mathbf{I}$  is the identity tensor,  $\mathbf{r} = \mathbf{X}_i - \mathbf{X}_j$  is the separation between an interaction pair, and the angle brackets signify an average over particles defined in Appendix B. The osmotic pressure is thence computed as

$$\Pi = -\frac{1}{3}\mathbf{I} : \boldsymbol{\Sigma}. \quad (9)$$

## 4 Results

The gel is formed as described in Section 2 from a dispersion of Brownian spheres at an initial volume fraction  $\phi = 20\%$ , and attractive interparticle potential of magnitude  $V_0 = 5kT, 6kT$  after which it is subjected to a gravitational field — a body force exerted on each particle,  $Pe = (4\pi/3)\Delta\rho ga^3/(kT/a)$ , varied to test the influence of particle weight,  $\Delta\rho g = (\rho_{particle} - \rho_{fluid})g$ , on collapse. The macroscopic deformation, microstructural evolution, and rheology are monitored throughout simulation. The resulting data are presented and analyzed here, starting with macroscopic deformation, followed by detailed structural analysis, then examination of bond dynamics and osmotic pressure.

### 4.1 Macroscopic collapse

Prior to application of the external force, the gel network spans the entire container with a structure that is homogeneous<sup>8</sup> over the network length scale. The external force is imposed and, over time, the gel eventually separates from the ceiling, forming a free

surface that descends downward. Utilizing the method described in Appendix A, the region of the gel initially in contact with the ceiling was monitored over time and, from it, the evolution of macroscopic gel height was measured, revealing distinct temporal sedimentation regimes. The sedimentation rate is computed from the same data, and is compared below to the sedimentation of purely repulsive hard spheres, suggesting potential mechanisms underlying the collapse behavior.

#### 4.1.1 Densification

Gravitational compaction of the gel reduces its macroscopic height and increases its volume fraction, and one goal of the present study is to determine whether the former causes the latter, or vice versa. The intimate connection between the two bulk measurements is nowhere more important than the emerging free interface that descends over time, because the criterion by which it is defined is the volume fraction of particles in the topmost layer of the gel. As discussed in Section 3, the network-length scale roughness of the newly free surface requires partitioning of the gel into vertically stacked layers a few particles thick, and computation of a volume fraction averaged within each individual layer (each of which encloses at least 3000 particles):

$$\langle \phi \rangle(z) = \frac{\sum_i 4\pi a_i^3/3}{V_{layer}}, \quad (10)$$

where the angle brackets denote an average over the layer centered at  $z$ , computed by adding the volume of every particle  $i$  located in the layer divided by the volume of the cuboidal layer,  $V_{layer}$ . We created 100 such bins, and these bins can either remain static or the bins can compress and follow the gel as it falls. The resulting depth-dependent volume fraction is plotted in Figure 3a for a  $5kT$  bond-strength gel and particle weight  $Pe = 0.05$  (plots for  $V_0 = 6kT$  and other values of  $Pe$  can be found in Figure S2 of the Supplementary Materials). Each curve shown is an instantaneous snapshot of  $\langle \phi \rangle(z)$  at selected times as noted in the legend. The initial volume fraction is  $\langle \phi \rangle = 20\%$ , for all depths  $0 \leq z/H \leq 1$ . Fluctuations in volume fraction correspond to the bi-continuous morphology of the gel comprising particle-poor pores and particle-rich strands. As the gel compacts, a depletion region forms near  $z/H = 1$  and an accumulation region near  $z/H = 0$ , forming three distinct zones distinguished by volume fraction: a colloid-poor region at the top with  $\langle \phi \rangle < 20\%$ , a free-falling zone in the middle with  $\langle \phi \rangle \approx 20\%$ , and a densifying zone at the bottom, with  $\langle \phi \rangle > 20\%$ . As the gel peels away from the ceiling, a supernatant forms where  $\langle \phi \rangle \rightarrow 0$ ; some particles are left behind stuck to the ceiling, giving  $\langle \phi \rangle \neq 0$  there.

As the gel densifies, a few particles remain attached to the ceiling, and others diffuse freely in the supernatant, while most of the particles remain with the bulk gel. In Figure 3b, volume fraction is plotted from the bottom of the container to the current height of the gel,  $h_{gel}$ . The “free-falling” and densifying zones, predicted by Buscall and White<sup>32</sup> for strong gels, are clearly distinguishable but, in contrast to their permanently-bonded gel, the volume fraction profiles in Figure 3b show pronounced spatial and temporal variation. First, the interfacial region with  $\langle \phi \rangle < 20\%$  is not sharp and can penetrate down to 10% of the bulk gel. Sec-

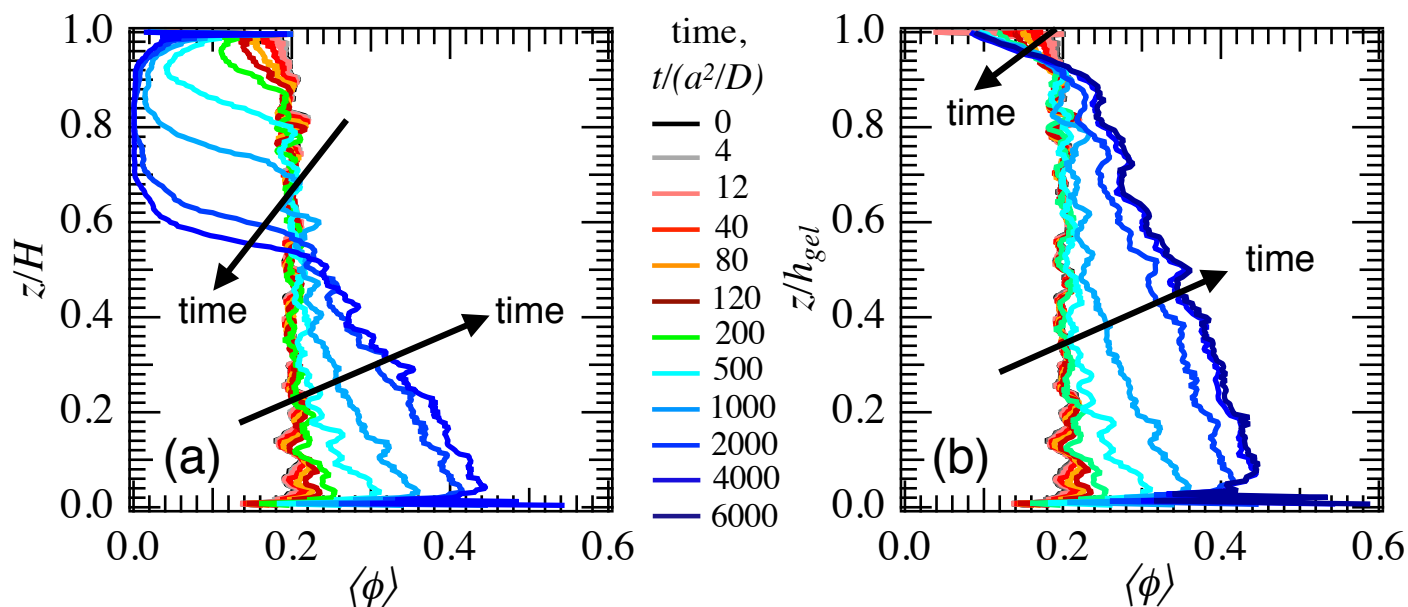


**Fig. 3** Layer-by-layer evolution of volume fraction in horizontal slices at various times spanning the duration of collapse for  $V_0 = 5kT$ , for particle weight  $Pe = 0.05$ . (a) Layers span the simulation cell, floor to ceiling. (b) Layers span only the current height of the gel.

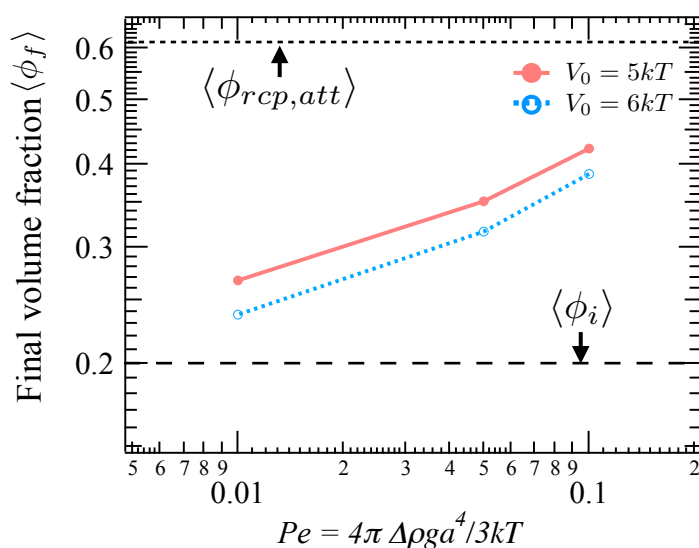


**Fig. 4** Final average volume fraction,  $\langle\phi_f\rangle$ , after collapse. Dashed and dotted horizontal lines show initial average volume fraction  $\langle\phi_i\rangle$ , and volume fraction of an attractive hard-sphere colloidal glass,  $\langle\phi_{rcp,att}\rangle$  respectively.

ond, density fluctuations within the free-falling zone change over time, demonstrating that the gel is not truly in free-fall. That is, the relative positions of particles within layers are evolving with time, unlike that of a permanently bonded gel. In particular, an increase in volume fraction near  $z/h_{gel} = 0.4$  reveals densification in the middle region of the gel, suggesting for the first time that densification may arise not only due to affine compaction, but also due to some other driving force. This is the first indicator that phase separation may play a role in gel collapse.

The middle and bottom zones, initially differentiable as

$\langle\phi\rangle = 20\%$  and  $\langle\phi\rangle > 20\%$ , merge at long times and, concomitantly, densification slows markedly. The final volume fraction at the free surface is approximately 10%, and is  $30\% \leq \langle\phi\rangle \leq 45\%$  elsewhere. A coarse estimate of the final compacted volume fraction is obtained by an average over the entire compacted gel,

$$\langle\phi_f\rangle = \frac{1}{h_{gel}} \int_0^{h_{gel}} \langle\phi\rangle(z) dz. \quad (11)$$

Prior studies<sup>22,24</sup> noted that weaker bonds permit denser compaction, which we study here by varying bond strength  $V_0/kT$  and particle weight,  $Pe$ . We plot the final volume fraction  $\langle\phi_f\rangle$  in Figure 4 for a range of particle weights  $0.01 \leq Pe \leq 0.1$ , and two interparticle strengths,  $V_0 = 5kT$  and  $V_0 = 6kT$ , which are expected to lie between the volume fraction of the undeformed gel  $\langle\phi_i\rangle = 20\%$ , and the volume fraction of an attractive glass  $\langle\phi_{g,attr}\rangle \simeq 62\%$ .<sup>41–43</sup> The final height for the range of particle weights and bond strengths spans the range  $25\% \leq \langle\phi_f\rangle \leq 45\%$ , with a more densely packed terminal gel state as  $Pe$  increases. If we recall the phase diagram in Figure 1, the final compacted gel would now be located farther to the right, possibly outside the binodal. This suggests that yield is a non-equilibrium leap to a region of more complete phase separation. Weaker interparticle bonds permit a greater leap; this suggests that re-arrest of phase separation, rather than mechanical equilibrium, determines when compaction will stop.

Overall, the evolution of volume fraction shows that bond reversibility plays a qualitative role in compaction mechanics. The volume fraction within the gel also contradicts the idea that collapse causes disintegration of the network into clusters which subsequently pack closely in a final sediment. In the present study, this is evidently not the case, since the average volume fraction does not reach random-close packing. This suggests that the gel retains its continuous network structure throughout the duration

of collapse; a detailed analysis of its structure is undertaken in Section 4.2. Finally, the final volume fraction represents a leap outside the binodal in the phase diagram, strongly suggesting a phase separation process that subsequently re-arrests.

#### 4.1.2 Bulk height evolution

Slow descent of the bulk height commences after application of the external force and is monitored over time, utilizing the algorithm described in Appendix A. The temporal evolution of gel height changes with particle weight,  $\Delta\rho = \rho_{particle} - \rho_{fluid}$ , and is studied here over the range  $0.01 \leq Pe \leq 0.1$ , selected to correspond to experimental studies.<sup>15–19,21,22,26,44</sup> The instantaneous height of the gel  $h_{gel}$ , normalized on its initial value  $H$ , is plotted as a function of time in Figure 5a. Several curves are shown, corresponding to the range of  $Pe$  indicated in the legend, with two curves for each value of  $Pe$ : one for  $V_0 = 5kT$  and one for  $V_0 = 6kT$  bond strength.

All curves in Figure 5a display a monotonic decrease of gel height over time, where changes in slope recover three well-defined regimes: slow initial compaction, a subsequent period of rapid sedimentation, followed by a slower, long-time compaction regime. The simulation results here show excellent qualitative agreement with experiments.<sup>15–19,21,22,26,44</sup> Even with the simple model of a freely draining gel, we recover all the hallmarks of gel collapse.

The initial compaction of the gel during the induction period\* is quite small when plotted within the range of the overall height. The inset shows a zoomed-in view of the induction period on a linear-linear scale, showing that initial deformation is indeed small,  $0.1\% \leq h_{gel}/H \leq 0.5\%$  (this deformation is at least an order of magnitude larger than the resolution of the measurement algorithm described in Appendix A, which can detect bulk strain as small as 0.01%). The slow descent eventually transitions to faster deformation, where the change in slope signals the end of the induction period. This “delay time”,  $\tau_{delay}$ , between forcing onset and rapid sedimentation, shortens as the forcing strength increases.

The decrease in delay time with increasing  $Pe$  is shown in Figure 5b, for both the  $5kT$  and  $6kT$  gel, and recovers experimentally reported trends.<sup>17,21,22,24,31</sup> The two curves are well separated when  $Pe$  is small, suggesting that Brownian motion and thus bond dynamics play a role in the delay time. Indeed, weaker attractions are correlated with a shorter delay time and this disparity widens as forcing gets weaker, showing that at the same value of  $Pe$ , stronger Brownian motion hastens collapse. This dual trend has been studied in prior theory and experiments and has been attributed to an increased bond rupture rate<sup>21</sup> that leads to loss of network connectivity, or a decrease in bond formation rate that interferes with concurrent gelation and sedimentation,<sup>16</sup> in turn leading to rapid sedimentation. While such studies provide convincing support for the idea that external forcing augments thermally activated bond rupture and can be utilized to predict

the delay time, no detailed structural measurements have been made to support the ideas. Our recent study of fixed-stress shear yield showed that Brownian motion hastens yield.<sup>1</sup> In Section 4.3 we present measurements of bond loss and gain, along with other structural changes, to interrogate the cause of the delay in yield.

The second regime, fast sedimentation, is well-separated from the first regime by a finite transition from shallow to steep slope in the height-evolution curve. The transition region is examined both to identify the delay time,  $\tau_{delay}$ , between gelation and collapse, and also to characterize the onset of collapse as “abrupt”<sup>16,21</sup> or “gradual”<sup>17,31</sup>. The former objective is typically carried out by setting  $\tau_{delay}$  to the time at which lines drawn tangent to the slow-induction and fast-sedimentation regimes intersect. The latter observation (abrupt versus gradual) leads to conjecture about the mechanistic cause of the transition to fast collapse, and is simultaneously the most interesting and least understood aspect of gel collapse. Hypotheses vary widely, such as a loss of network connectivity,<sup>22</sup> the widening of network channels during the initial induction period,<sup>17</sup> detachment of the gel from the meniscus,<sup>18</sup> and fluid backflow that ruptures the network.<sup>16</sup> At a minimum, it can be said that the gradual steepening bears the hallmarks of a “tipping point”, but visual inspection does not provide satisfying insight to the underlying micromechanics. In the present study, structural changes accompanying this rheological transition are interrogated in detail in Section 4.2 to obtain precise temporal connection between onset of rapid sedimentation and structural evolution.

Rapid sedimentation is the next temporal regime of gel collapse, where the majority of bulk height is lost over a time scale much shorter than the initial delay, as shown in Figure 5a. The inset reveals that when interparticle bonds are strong and particles are not heavy, the fast collapse appears short-lived.

At long times, sedimentation slows, approaching a plateau. The change in height approaches zero, giving a long-time “final” sediment height. Unsurprisingly, weaker interparticle bonds and heavier particles both permit a more compacted final sediment, consistent with experiments<sup>22,24</sup> and the average final volume fraction calculations in Section 4.1.1.

Overall, we have demonstrated that a simple freely draining model recovers the three distinct temporal collapse regimes: a slow induction period that ends with a tipping point, followed by a transition to faster sedimentation; then rapid sedimentation over an extended period of time and, finally, slow, long-time compaction. Small changes in height preceding the tipping point, and the dependence of delay time on bond dynamics suggest that small but quantifiable structural changes underlie the tipping point. The model recovers experimentally reported dependence of delay time and final compaction height on  $Pe$  and bond strength and show that bond reversibility plays a qualitative role in collapse mechanics. In the following sections, we will interrogate the evolution of sedimentation rates and examine the snapshots accompanying the regimes of sedimentation.

#### 4.1.3 Sedimentation rate

Detailed measurements of macroscopic height taken in Section 4.1.2 permit accurate computation of the transient sedimentation

\*A non-uniform descent of the gel in the early stages of the induction period may be present in some experiments in which the gel slides along a curved meniscus to which it is initially attached.<sup>17,18</sup>

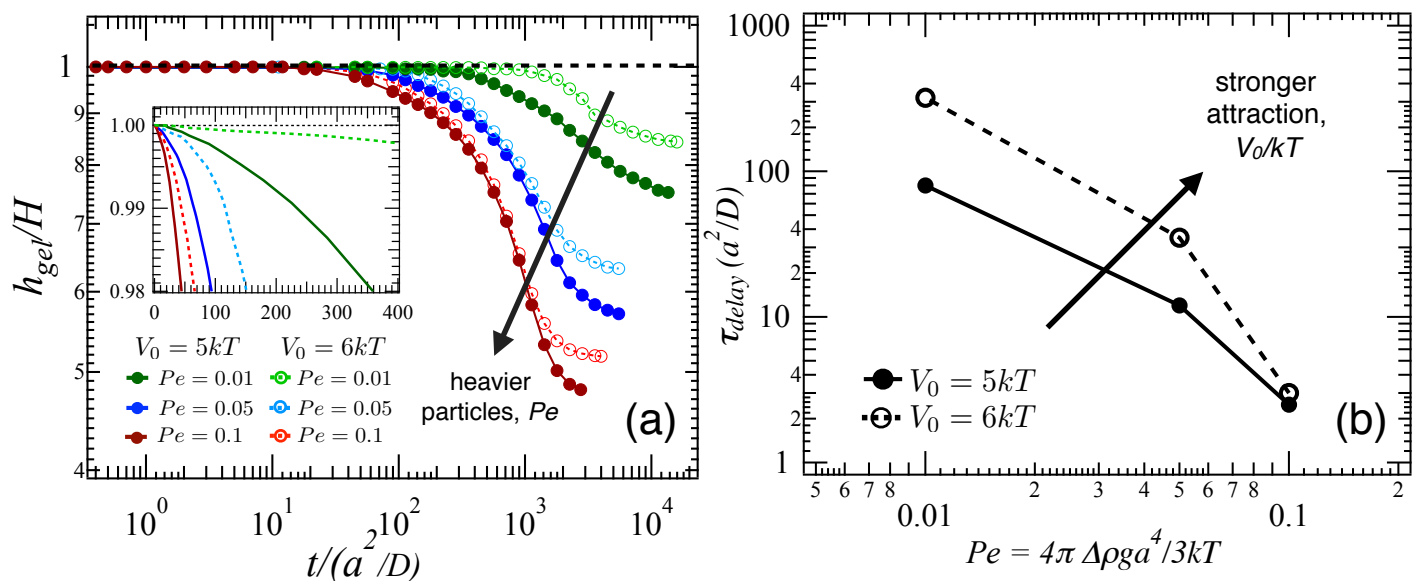


**Fig. 5** Macroscopic response. (a) Descending gel height normalized on its initial value, following onset of gravity. Time is scaled diffusively. (b) Delay time,  $\tau_{delay}$  made dimensionless with the timescale of Brownian motion.

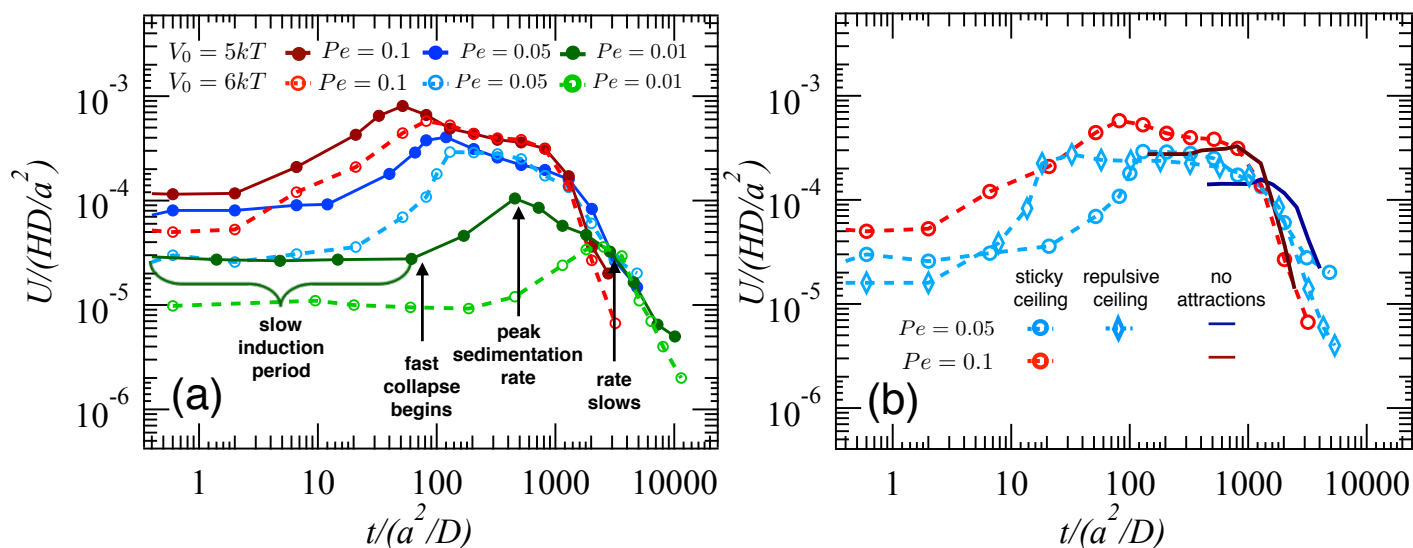


**Fig. 6** Sedimentation rate  $U \equiv -dh_{gel}/dt$ , normalized on  $HD/a^2$ , as a function of time, (a) computed from height evolution data in Figure 5a. (b) Comparison to purely repulsive floor/ceiling, and to purely repulsive, freely draining particles.

tation rate and thus enable quantitative analysis of the tipping point and qualitative understanding of whether the network settles like a suspension (of particles or clusters) or condenses by some other mechanism.

The sedimentation rate  $U$  is computed as the slope of the temporally evolving height, and is plotted in Figure 6a as a function of time, for a range of particle weights  $0.01 \leq Pe \leq 0.1$ . The temporal regimes characteristic of delayed sedimentation<sup>15–27</sup> are recovered in all curves: First, a constant compaction speed is observed at short times, the induction period. A sudden increase in  $U$  is identified as the tipping point, which permits the gel to enter the fast collapse regime. It reaches a peak value that increases and occurs earlier as  $Pe$  increases and as bond strength decreases. Eventually, the sedimentation rate slows markedly, entering long-time compaction slower than initial compaction. The shortening of delay time with weaker bonds is less pronounced than the effect of increased particle density,  $Pe$ , suggesting that the delay time does not simply span a period of ceiling detachment.

To test the influence of gel attachment to the ceiling, additional simulations were run with a purely repulsive ceiling. Figure 6b illustrates this effect on the sedimentation rate for a  $6kT$  gel with  $Pe = 0.05$ . The delay time is shorter by a scalar value without the attachment, but collapse still exhibits a pronounced delay, confirming that collapse is a bulk rheological phenomenon. Although an attractive interaction with the container or a stiff meniscus decreases the initial sedimentation rate, it does not suppress the induction period, showing that colloid-colloid interactions underlie the delay time.

It is natural to ask whether the neglect of hydrodynamic interactions makes the sedimenting gel the same as a sedimenting dispersion of purely repulsive colloids. We measure the rapid-phase sedimentation rate and compare it to a freely draining suspension undergoing sedimentation in a finite-height container. As particles advect downward and accumulate near the bottom, the resulting number-density and osmotic-pressure gradient drive diffusive flux upward. Sedimentation rate curves in Figure 6b illustrate the downward particle flux: in the absence of interparticle bonds, the topmost layer undergoes constant free fall from  $\hat{t} = 0$  until the accumulation region at the bottom drives gradient diffusion upward, in turn slowing overall sedimentation. The most important feature to notice is that for the purely repulsive hard-sphere dispersion, there is no tipping point, no appreciable increase in fall speed, and no induction period. *Delayed collapse requires bonds, but does not require hydrodynamic interactions.*

Remarkably, the purely-repulsive suspension falls slower than a gel subjected to the same gravitational forcing. This can be understood by recognizing that for purely repulsive particles, osmotic pressure is positive, giving a tendency for the particle-phase to expand outward,<sup>45</sup> thereby resisting gravity and slowing sedimentation. When particle attractions are strong enough to induce gelation, the contribution to osmotic pressure from interparticle interactions (i.e. the second virial coefficient) is negative on average,<sup>8</sup> pulling particles toward one another, condensing the particle phase, thus aiding compaction. Quantitative analysis (Figure S5 in Supplementary Materials) shows that when bonds are stronger, the scaling with  $Pe$  increases. This result is coun-

terintuitive if one expects stronger bonds to produce a stronger gel network, i.e., that stronger bonds give a higher yield stress. We will return to the idea in Section 4.4 that the sign of osmotic pressure determines the tendency of the material to compact.

To understand this surprising result, one can recognize that the elastic stress,  $n\langle xF^P \rangle$ , produces a negative osmotic pressure in the presence of attractive forces, becoming more strongly negative as bonds become stronger. This suggests that the same negative osmotic pressure that drives condensation and phase separation is driving the collapse of a kinetically arrested gel, but a state of arrest slows the rate of response (fall speed) of the gel. From this we might infer that yield is a release from kinetic arrest, that collapse is actually condensation, i.e., non-equilibrium phase separation, and that the “tipping point” to fast collapse is the onset of this phase separation.

In summary, gel collapse is a bulk rheological phenomenon whereby an evidently intact, self-supporting network yields and sediments. The durable but transient bonds produce compaction that is distinct and indeed faster than the settling of a dispersion of unbonded particles, which we hypothesize arises from the negative osmotic pressure created by a condensing particle phase. Overall this suggests that non-equilibrium phase separation is the central process underlying the delay and tipping-point behavior.

## 4.2 Structural evolution

In the previous section, a phenomenological picture of gel collapse emerged in which yield signals a release from kinetic arrest and collapse is gravity-activated, non-equilibrium phase separation; here structural measurements are made to interrogate this idea. Prior studies have put forth other phenomenological descriptions of the structural evolution underlying the macroscopic induction and bulk collapse phases. To support our claim that activated phase separation is the fundamental mechanism at work, we begin with simple visual inspection of the microstructure at key instants during gel collapse. A series of snapshots of the structure is embedded in the plot in Figure 7, each taken at the time  $\hat{t} \equiv t/(a^2/D)$ , connecting structure to the bulk sedimentation curve for  $Pe = 0.05$  and  $V_0 = 5kT$  (Images for  $V_0 = 6kT$  and other  $Pe$  can be found in Figures S3 and S4 of the Supplementary Materials). For this gel, the induction period extends from  $0 \leq \hat{t} \leq 12$ , with peak sedimentation occurring at  $\hat{t} = 120$ , fast collapse until  $\hat{t} \approx 1400$ , and finally, slow, long-time compaction.

At  $\hat{t} = 0$ , the network appears fully connected, and forms an elastic gel<sup>†</sup> that is bonded to the top and bottom surfaces, spanning the entire container. The next snapshot is taken at  $\hat{t} = 12$ , corresponding to the end of the induction period, and shows no visually obvious structural change during the delay time. The gel remains fully attached to the ceiling, the network appears to remain connected, and morphology unchanged. These observations are unsurprising on one hand, given that the bulk deformation measurements presented in Section 4.1.2 show less than 0.5%

<sup>†</sup>  $G'$  and  $G''$  measurements in the linear regime over frequencies reveal that the elastic modulus of the network dominates over its viscous modulus. See Figure S1 in Supplementary Materials.

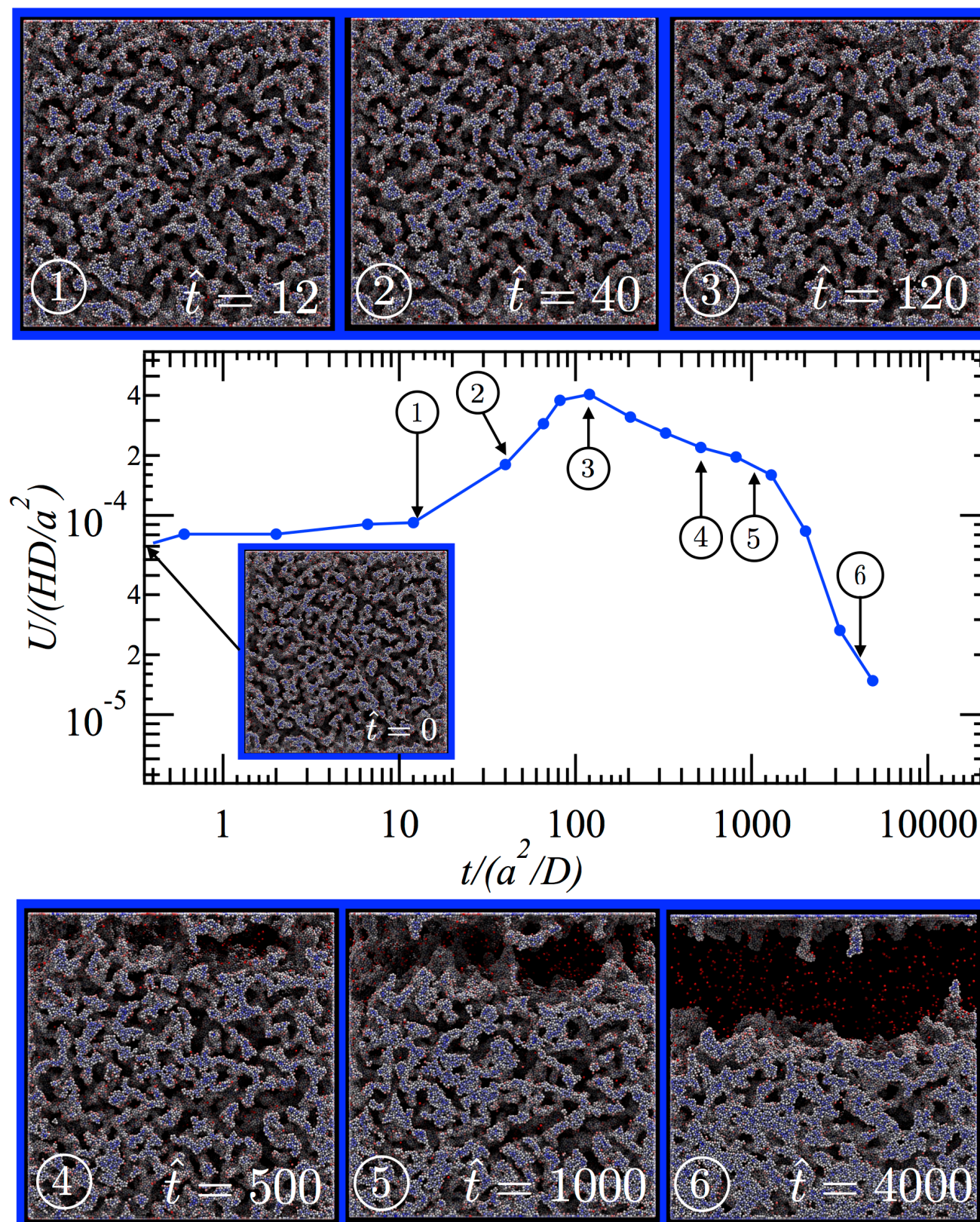


**Fig. 7** Sedimentation rate  $U \equiv -dh_{gel}/dt$ , normalized on  $HD/a^2$ , plotted as a function of diffusively scaled time for gel with bond strength  $V_0 = 5kT$  and particle weight  $Pe = 0.05$ . Snapshots of the gel at several instants during the sedimentation process.

bulk strain. However, this result is remarkable in the context of prior phenomenological models put forth to explain the end of the delay period such as break-up of the network into clusters,<sup>22</sup> or breakage of strands and release of debris from the network<sup>17</sup>. The lack of network-length scale rearrangement during induction suggests that bulk deformation during induction must be carried out by individual particle displacements.

The layer of particles adjacent to the ceiling is examined to see whether the gel detaches everywhere at the same time, or more gradually. The height detection algorithm (Appendix A) provides a means by which to characterize the developing rough interface, where spatial resolution of volume fraction measurements detect both particles and pores. Solvent pores adjacent to the ceiling are depicted as contour maps in Figure 8. As shown in the legend, bright green cells correspond to particle-rich regions near the container surface, while gray regions correspond to solvent pores near the container surface, and black indicates vertically deep pores of a dozen particle radii. At  $\hat{t} = 0$  (Figure 8a), most of the ceiling is covered by particles, separated by a few shallow pores. At the end of the induction period, at  $\hat{t} = 12$ , more pores of the same vertical size appear adjacent to existing pores, indicating that pores adjacent to the ceiling grew laterally but not vertically. Initial depletion of the top layer of the gel similarly measured in experiments<sup>17</sup> also occurs by lateral pore enlargement rather than average bulk descent.

To understand the lateral pore growth mechanism during the induction period, we revisit the mechanism of pore growth during quiescent aging. The durable yet temporary nature of bonds allows the gel to restructure over time;<sup>8</sup> net migration of particles is driven by decrease of potential energy, as illustrated in Figure 9. A cross-sectional sketch of a network junction in Figure 9a depicts two types of curvature — axial curvature along the strand, and hoop curvature around the strand. Idealized particle-scale structure for a strand with a smooth surface is depicted in Figure 9b; the mobile surface particles have more bonds when they reside at a junction, and fewer bonds far from a junction. Curvature thus produces a driving force for particles to migrate away from the strand and toward the junction, eventually dissolving the strand. Such migration is enhanced further (cf Figure 9c) by hoop curvature, driving particles away from continuously narrowing strands. This exposes a new, higher-energy free surface comprising particles with fewer bonds, driving even faster pore growth. Overall, this quiescent-aging driving force is self-reinforcing, causing pore growth and thickening of strands by particle migration toward junctions in the network.

Particles in contact with the ceiling can only migrate downward or laterally, illustrated in Figure 9d. For a pore surrounded by particles adjacent to the ceiling, particles closest to the ceiling have the highest energy. At short times, they migrate away from the ceiling toward the bottom of the pore, decreasing energy and causing lateral pore growth. Weak gravitational forcing further enhances this migration. Some particles may also dislodge from the surface and be advected by gravity toward the bottom of the pore to cause further lateral pore growth during induction. The slow descent of the gel during the induction period is thus caused by gravity-enhanced coarsening migration that leads to

self-reinforcing lateral pore growth near the ceiling.

The tipping point is essentially the result of a capillary-type instability, where particles migrate away from the length of a strand toward a junction. Owing to the strong influence of Brownian motion, this instability manifests as a transition from pore widening to rapid vertical pore growth, rather than a dramatic disintegration of the entire network.

As sedimentation speed ramps up from the tipping point to the peak fall speed ( $12 < \hat{t} \leq 120$ ), Figure 8c-d show that several portions of the gel are still attached to the ceiling, even at  $\hat{t} = 120$  (well into rapid sedimentation). That is, neither the tipping point nor the peak sedimentation is set by the gel simply letting go of the ceiling. Further, new gray cells appear, as pores continue to grow laterally, revealing that self-reinforcing pore growth and coarsening continue beyond the tipping point, and the instability grows. Additionally, vertical pore growth commences (dark grey cells), as some particles dislodged from the network surface migrate downward under gravity toward the bulk. Zoomed-in view of the top several layers in the gel and quantitative volume fraction measurements (in Figures S6 and S7 in the Supplementary Materials) provide further support.

Our results agree with observations reported in the experimental literature, which show that rapid sedimentation begins while the gel is still partially attached to the top boundary. For example, Starrs *et al.*,<sup>18</sup> provide dark-field images of the collapsing gel that show that the gel slides partly down the meniscus at very early times, then detaches only partially during the induction period. These images are compared to corresponding times on the height vs time plot (at arrow 'j') and show that the gel is still clearly and partially attached to the meniscus at the onset of rapid sedimentation. Similarly, video of gel collapse from Kamp and Kilfoi<sup>22</sup> show the emergence of a rough interface, but the correspondence between the images, height, and time was not presented. What is clear from their video is that backflow and recirculation occur well after onset of collapse. Overall, experiments agree with our findings: collapse is not a simple matter of a gel that is too weak to sustain its own weight once it detaches from supportive boundaries.

Recent simulation studies by Del Gado and coworkers<sup>46</sup> have shown that in the limit of very weak thermal motion where gel morphology is stringy with low average contact number, strands rupture where local stresses are high in the network. The consequence of rupture is stress relaxation over long length scales in the network that can be screened by increasing thermal motion. In the present study where thermal motion plays a significant role in particle rearrangements and morphology is bi-continuous and strands are thick, strand dissolution occurs from particle motion, over many Brownian times, leading to the formation of a rough surface, which in turn drives even more particle migration toward lower energy.

Following the peak sedimentation rate, structural changes are pronounced and visually obvious, as shown in snapshots of the entire gel in Figure 7. During the rapid sedimentation regime, at  $\hat{t} = 500$ , gradual dissolution of strands near the top leaves colloid-poor regions several particles deep, separated by strands still attached to the ceiling. By  $\hat{t} = 1000$  (Figure 7), the colloid-

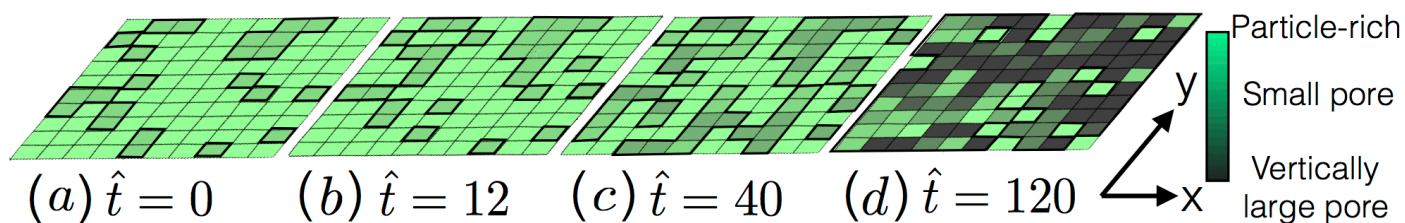


**Fig. 8** Contour map of pores adjacent to ceiling showing the gel formed by  $V_0 = 5kT$ , forced at  $Pe = 0.05$  at a variety of instants in time from the onset of gravity until peak sedimentation rate. Green cells corresponds to regions where particles are attached to the ceiling, and gray cells correspond to pores adjacent to the ceiling. Gray-scale shows the depth of the pore from the ceiling, with darker color indicating vertically larger pore.

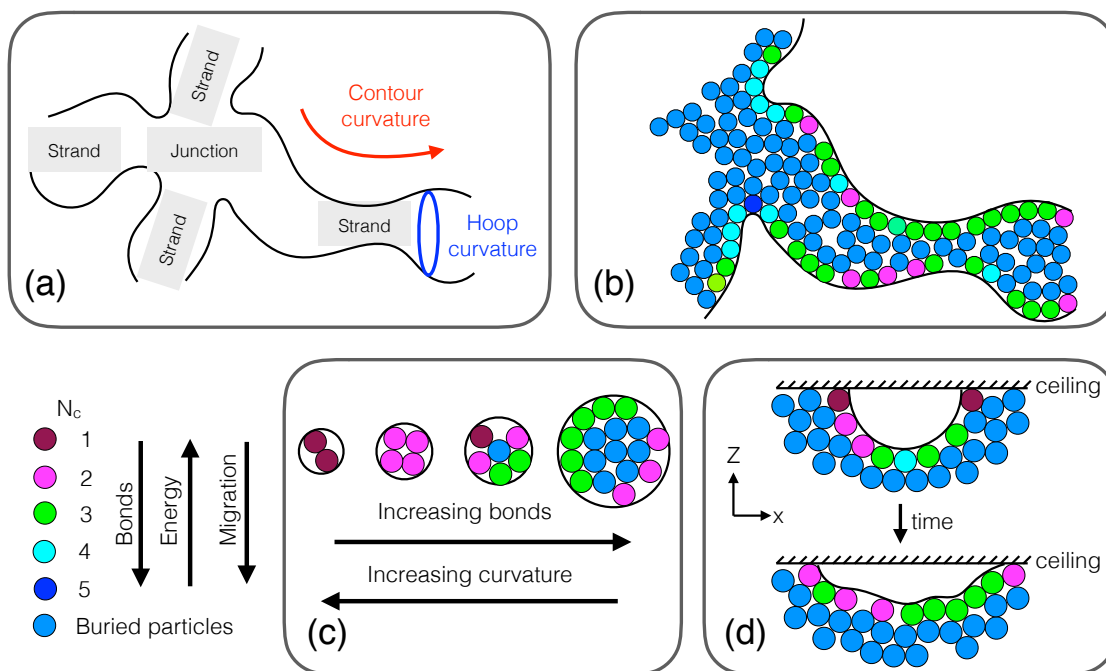


**Fig. 9** Illustration of the driving force causing particles to migrate toward junctions in the bulk, and away from the ceiling near the top. On average, particles migrate from fewer bonds (high energy) to more bonds (low energy). (a) Typical structure of a junction in a gel. (b) Illustration of particle positions colorized by their  $N_c$  along strand. (c) Illustration of particle positions colorized by their  $N_c$  around strand. (d) Illustration of pore widening adjacent to the ceiling.

poor regions grow and more strands dissolve but the rough surface is still partially attached to the ceiling. A container-wide supernatant does not emerge until much later. That is, neither the tipping point, peak sedimentation rate, nor rapid sedimentation requires detachment of the gel from the ceiling, and the gel can descend rapidly even when a significant portion is still attached to the ceiling.

While the gel descends away from the ceiling, particles accumulate near the bottom (Figure 3b and zoomed-in volume fraction measurements in Figure S7 in Supplementary Materials), where morphology changes include pronounced pore shrinkage (Figure 7). Nonetheless, the entire gel retains its porous network structure, contrary to the hypothesis<sup>15,16,22</sup> that the network ruptures into clusters that subsequently pack densely near the bottom of the container.

A container-wide supernatant appears by  $\hat{t} = 4000$  (Figure 7), where the entire gel is detached from the ceiling, save the lone particles and dangling strands remaining attached to the ceiling. The most important feature of gel morphology is the interface separating the gel and the supernatant, which is still rough at the length scale of the container. Quantitative measurements of volume fraction support the visual observation of a container-wide supernatant (see Figure S7 in Supplementary Materials) where  $\langle\phi\rangle \rightarrow 0$  at  $\hat{t} > 1000$ . The interfacial region (Figures 3b and S7 in Supplementary Materials) thins over time, with the  $\langle\phi\rangle \simeq 20\%$  region creeping slowly upward toward  $z/h_{gel} \simeq 94\%$ , and the topmost layer at  $\langle\phi\rangle \simeq 10\%$  and slowly depleting. The middle zone has disappeared. By this time, the sedimentation rate decays rapidly and collapse ceases, indicating that when the gel can densify no further, collapse stops.

Overall, structural evolution is reminiscent of a capillary-type instability triggered by gravity, where the particles near the ceiling migrate away from strands toward junctions, leading to a transition from lateral pore growth to vertical pore growth at the tipping point. The onset of this instability should be quantifiable by bond dynamics, where the transition to vertical pore growth beyond the tipping point is signaled by a decrease in average bondedness that subsequently reverses, owing to coarsening and restructuring of the interface. When fast collapse is underway, the bulk of the gel undergoes pore shrinkage and densification; macroscopic sedimentation rates are fast compared to purely repulsive freely draining hard spheres, suggesting that a mechanism other than simple advection toward the impermeable floor drives the gel downward. Similar to the driving force near the interface, enhanced coarsening migration in the bulk can also cause the gel to eliminate bicontinuous structure and increase volume fraction, a condensation process. Bond dynamics in the bulk and near the top surface are interrogated in the next section to quantify and test these ideas.

### 4.3 Bond dynamics and evolving the energy landscape

Here we interrogate bondedness, potential energy, and volume fraction throughout the simulation to shed light on the driving forces of delayed gel collapse. The rate process that connects each of these to one another and to phase behavior is bond dy-

namics — how and when particles gain or lose bonds relative to the three temporal regimes of collapse, and the potential energy landscape this creates. The microscopic bond dynamics within the three macroscopic spatial regions (rough surface, free-falling bulk, compacting bottom) are monitored to differentiate between enhanced coarsening and affine compaction, where the former is driven by phase separation and the latter is driven directly by gravitational flux. The osmotic pressure is a complementary measurement that will be utilized to distinguish phase separation-driven condensation from affine gravitational flux-driven compaction.

#### 4.3.1 Average bond evolution: minimization of potential energy

Reversible gelation creates durable bonds between particles that can rupture to permit diffusive particle migration along gel strands, where a particle exchanges neighbors but eventually acquires more bonds; dynamics thus slow and arrest deepens in this process of age coarsening.<sup>8</sup> The sketch in Figure 9 illustrates how this process is driven by the bond-energy landscape, driving instability of the network away from strands toward junctions, which favors formation and relaxation of bonds. Here we examine the effect of gravitational forcing on this process, by monitoring interparticle separation throughout simulation, and using it to track bond formation, bond loss, and changes in potential energy. The measurement underlying each of these is interparticle separation,  $s = (r - 2a)/2\Delta$ , which is monitored for each neighboring pair throughout simulation. When  $s \leq 1$ , the pair is bonded. Each particle thus has a contact number,  $N_c$ , arising from all the bonds that connect it to its neighbors. Summing  $N_c$  over all particles and dividing by two gives the total number of interparticle bonds. Bond formation and loss are tracked via the contact number, with  $N_c = 0$  for free diffusers,  $1 \leq N_c \leq 7$  for particles on the surface of network strands, and  $8 \leq N_c \leq 12$  for particles buried deep within a strand. There is thus a well-defined distribution  $P(N_c)$ , average  $\langle N_c \rangle$ , and peak value of contact number that correlate with morphological features such as network surface-to-volume ratio. These can each be computed utilizing the entire gel population, or within spatial regions, e.g., the horizontal slices as defined in Section 4.2. Once a bond is formed, it can be stretched, relaxed, or compressed. The precise length  $s$  of a bond sets the potential energy of a pair interaction. A decrease of potential energy indicates of bond relaxation or gain, while potential energy increases as a bond moves away from equilibrium — either stretching or compressing. Each condition is identified by the sign of  $s$ . The average potential energy per particle is thence computed as a sum over all bonds, divided by the number of particles  $N$ :

$$\langle PE \rangle(t) = \frac{\sum_{i < j} V_{ij}(r_{ij})}{N}. \quad (12)$$

Changes in potential energy accompany phase transitions in molecular materials, as part of the Helmholtz free energy minimization that drives spontaneous processes. Equilibrium colloidal phase transitions have been treated similarly,<sup>3,47</sup> with success. Here we propose to examine changes in the average potential energy of the gel during yield and densification, with the view that

decreasing  $\langle PE \rangle$  is one indicator of progression toward equilibrium, i.e., release from kinetic arrest. Normalized on its initial value,  $\langle PE_0 \rangle$ , a value of  $\langle PE \rangle(t)/\langle PE_0 \rangle$  greater than unity corresponds to increasingly negative (decreasing) potential energy (bond formation and relaxation). When  $\langle PE \rangle(t)/\langle PE_0 \rangle < 1$ , existing bonds are either compressed or stretched (possibly lost), leading to an increased (less negative) potential energy. ‡

The gel is binned into nine layers of equal thickness that changes as the gel falls, and the contact number and potential energy are averaged within each layer (defined in Appendix B) and plotted in Figure 10. The average contact number and potential energy for a quiescently coarsening gel and for each layer in the falling gel are plotted in Figures 10a and 10b respectively. Shaded regions indicate bulk macroscopic regimes. The dotted quiescent curves reveal slow ongoing coarsening,  $\langle N_c \rangle(t)/\langle N_{c,0} \rangle > 1$  as bonds form; meanwhile,  $\langle PE \rangle(t)/\langle PE_0 \rangle$  increases with time.

In the top layer of the collapsing gel, the average contact number and potential energy show little change during induction, consistent with the findings in Section 4.2. However, the macroscopic transition regime (orange background) overlays precisely with a measurable shift in bond dynamics in the topmost layer in the gel. Beyond the tipping point, approximately 0.2% of bonds are lost, and the normalized potential energy increases (Figure 10b), suggesting that bond loss is accompanied by some bond stretching. That is, the capillary-type instability is set by average bond loss, which is what permits a transition from lateral to vertical pore growth. However, coarsening should ultimately result in an increase in number of bonds and a decrease in potential energy. Beyond the tipping point, initial bond loss is rapidly overtaken by net particle migration toward junctions and reattachment of particles in the network, leading to a subsequent decrease in potential energy ( $\langle PE \rangle(t)/\langle PE_0 \rangle > 1$ ) and an increase in number of bonds within the gel. This coincides with the dissolution of some ceiling-attached strands, and partial liberation of a free surface. The surface now rapidly smooths itself, giving the ramp-up to fast bulk descent. Quantitative microscopic support of this idea is shown in the curves spanning the transition regime ( $12 \leq \hat{t} \leq 120$ ), which reveal a reversal from average bond loss to average bond gain (Figure 10a), at  $\hat{t} = 100$ .

Following peak sedimentation ( $\hat{t} > 120$ ), the gel continues to detach from the ceiling (cf Figure 3b) where one expects that bonds must be lost in the creation of a free surface. Surprisingly, in Figure 10, the average contact number continues to increase while the average potential energy continues to decrease ( $\langle PE \rangle(t)/\langle PE_0 \rangle > 1$ ), revealing net bond formation and relaxation without densification, supporting the idea that the fast descent of the rough interface occurs by smoothing of its bumpy topology via coarsening migration of individual particles: network evolution of pore growth and pore coalescence in the top layer. Whether this coarsening migration is enhanced by gravity is a question we return to shortly.

In the bulk of the gel, we observed in Figure 3b (and Figure S7 in Supplementary Materials) that volume fraction increases from the bottom up, most evident at long times; this densification can arise at least in part from simple affine compaction; but such condensation may also signal phase separation. To distinguish between the two, we recognize that if affine displacements drive collapse, the average potential energy would increase ( $\langle PE \rangle(t)/\langle PE_0 \rangle < 1$ ) at long times as particles are pushed toward hard-sphere contact, driving particles out of the energy minimum. Microscopic measurements actually reveal the opposite trend: a decrease in average potential energy ( $\langle PE \rangle(t)/\langle PE_0 \rangle > 1$ ) in the blue colored region of Figure 10b. The gel not only densifies everywhere but does so with a lower average energy. Compared to the quiescent gel, the falling gel exhibits a more pronounced decrease in potential energy over the same duration of time, indicating that this energy decrease occurs faster than the deepening arrest of quiescent coarsening.

Overall, evidence of a rapid decrease in potential energy accompanying densification and a more rapid descent (cf Figure 6b) of a gel compared to a suspension of purely repulsive hard spheres, together suggest that gel collapse is driven by a non-equilibrium phase separation rather than affine compaction alone, toward a dense, lower-energy structure. Further interrogation of osmotic pressure will quantify the contribution of affine compaction in driving particles toward hard-sphere contact, which would contribute to a positive osmotic pressure, in contrast to the negative osmotic pressure associated with phase-separation driven condensation.

To further interrogate the idea that collapse is triggered phase separation, we turn our attention away from average quantities to the distribution of contact number,  $P(N_c)$ , to interrogate the exchange between populations of particles binned by contact number.

#### 4.3.2 Bond distribution: densification mechanisms

In Section 4.2, we argued that self-reinforcing pore enlargement driven by gravity-enhanced coarsening is a capillary-type instability that produces the tipping point to collapse, but the observed shift in average contact number was small. Microscopic evidence of this process should include a change in contact-number distribution similar to that observed during quiescent age coarsening, but with gravitational enhancement of bond rupture — the ratcheting of particles to higher contact number at a rate faster than the quiescent shift.<sup>8</sup> We recall that quiescent coarsening leads to progressively deeper arrest with no change in net volume fraction, but growing dense domains and solvent pores; in contrast, if enhanced coarsening leads to rapid phase separation and densification in the bulk of the gel, a rapid migration of particles to higher contact number should precede densification in the bulk of the gel. A rapid migration of particles to higher contact number should precede densification in the gel. The evolution of total average contact number (Figure S8 in Supplementary Materials) smears out too much detail. To distinguish coarsening migration with no volume fraction change from particle advection with densification, we evaluate the evolution of distribution of contact number,  $P(N_c)$ , layer-by-layer in the gel.

‡ Whether  $\langle PE \rangle(t)/\langle PE_0 \rangle < 1$  results from bond stretching or compression can be discerned by a negative or positive osmotic pressure and an examination of bond-length statistics.

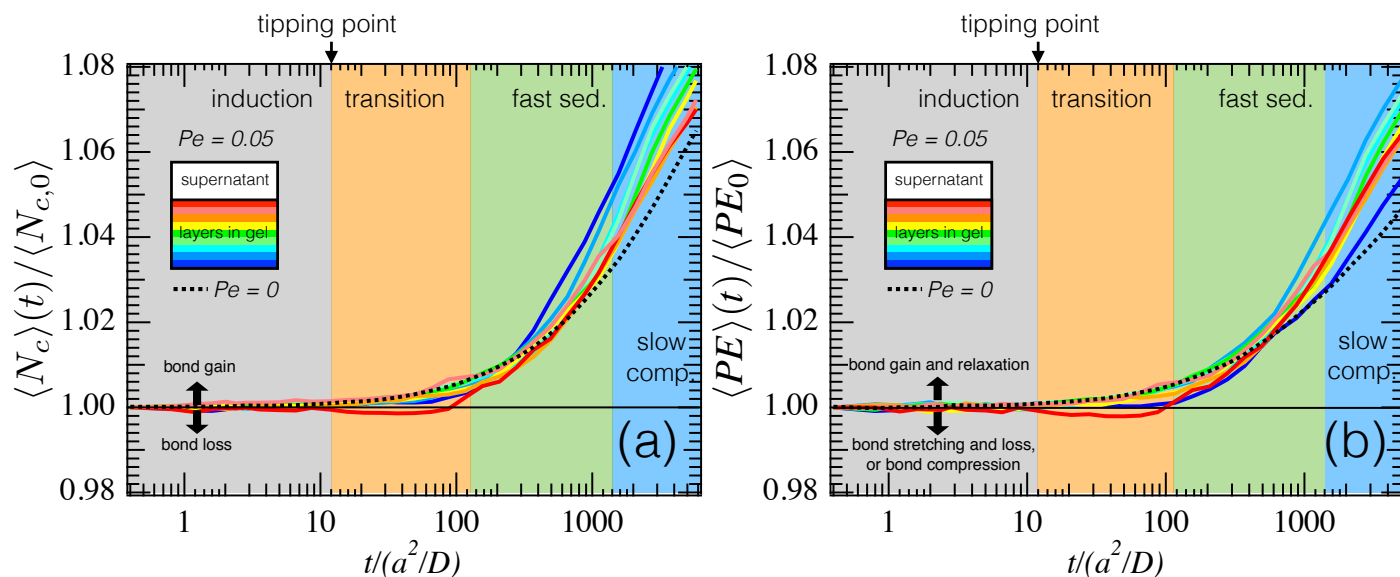


**Fig. 10** (a) Contact number and (b) potential energy density, plotted as a function of time. Black dotted curves correspond to values for a quiescent gel. Each colored curve corresponds to a layer within a falling gel with bond strength  $V_0 = 5kT$  and particle weight  $Pe = 0.05$ , where the color corresponds to a different depth in the gel, as indicated in the legend. Background color distinguishes temporal regimes for the falling gel.

Even though in Section 4.2 we saw growth in pore size, early-time changes in  $P(N_c)$  are difficult to distinguish, in agreement with  $\langle N_c \rangle(t)$ , because the mobile particles that drive coarsening belong to the population  $N_c \in [0, 3]$ , which constitute fewer than 4% of all particles in the gel. A small change in population of these particles is difficult to detect from  $P(N_c)$  curves,<sup>8</sup> but one can tease out the changes relative to the initial population size by normalizing the distribution at any time  $\hat{t}$  by its value at  $\hat{t} = 0$ , plotted in Figure 11. To get an even closer look, the gel is divided into three functional groups: the top 10% where it eventually detaches from the ceiling (plots (a) through (d)); a zone ( $0.4 \leq z/h_{gel} \leq 1$ ) in the gel that initially falls with no change in volume fraction until  $\hat{t} \leq 500$ , but undergoes densification beyond  $\hat{t} \gtrsim 500$  (plots e through h); and the bottom,  $0.1 \leq z/h_{gel} \leq 0.2$ , where particles accumulate near the sticky, no-flux floor (plots i through l). Each row corresponds to a spatial region. Each column is a temporal regime, corresponding to each shaded region in Figure 10.

The baseline is the change in contact number distribution for a quiescent gel. During early quiescent aging (first column), the top layer (plot a) sees a loss of low contact-number particles over time. At longer times ( $40 \leq \hat{t} \leq 120$ ), in the top layer (plot b), quiescent coarsening manifests as further decrease in populations of surface populations ( $1 \leq N_c \leq 6$ ) and a corresponding increase in populations of particles buried in the strand  $10 \leq N_c \leq 12$ , typical of the coarsening process where particles ratchet toward higher contact numbers. As the gel quiescently ages further (plots c, d), even more particles migrate toward high contact number, driving the peak of  $P(N_c)$  toward the right, consistent with previous detailed studies of quiescent coarsening.<sup>8</sup>

Now we examine changes in the falling gel starting with the topmost layer (Figures 11a-d). During the induction period ( $0 \leq \hat{t} \leq 12$ ), low-contact number populations  $0 \leq N_c \leq 3$  decrease and

the population corresponding to  $N_c = 4$  increases; while not visually dramatic, both are more pronounced than quiescent coarsening, supporting the view that the slow induction period occurs via enhanced pore growth arising from gravity-enhanced coarsening. This enhanced shift to higher contact number destabilizes the gel during the ramp-up period (Figure 11b); the growth of higher contact-number populations appears less pronounced than the decrease at lower contact number, owing to the disparity in overall population size (cf Figure S7 in Supplementary Materials). Recall that during the transition regime, a rough interface begins to emerge that eventually smooths itself via coarsening. Correspondingly, enhanced coarsening at the top layer continues into fast sedimentation and slow, long-time compaction, quantified by further particle migration from low contact-number populations to high contact-number populations in plots c and d. That is, the final formation of a flat interface with a smooth topology occurs via enhanced coarsening migration.

The bottom of the gel is always densifying and accumulating particles throughout collapse (cf Figure 3b). Here, the evolution of  $P(N_c)/P(N_{c,0})$  is markedly different compared to quiescent coarsening. During the induction period (plot i), the number of network surface particles with  $1 \leq N_c \leq 6$  decreases, accompanied by an increase in high contact-number particles (thickening strands). Beyond the tipping point (Figures 11j through l for  $\hat{t} > 12$ ), surface particles migrate toward higher contact number as expected, but, surprisingly, particles deeply buried in the strand  $N_c = 12$  migrate toward lower contact number, resulting in an increase in population  $N_c = 9$ . This results in pore shrinkage, signaling condensation. We recall that the bottom layer is always undergoing affine compaction because the floor is impermeable to particles, and the changes in  $P(N_c)/P(N_{c,0})$  observed could arise from either affine compaction or from activated phase separation in the bulk of the gel.

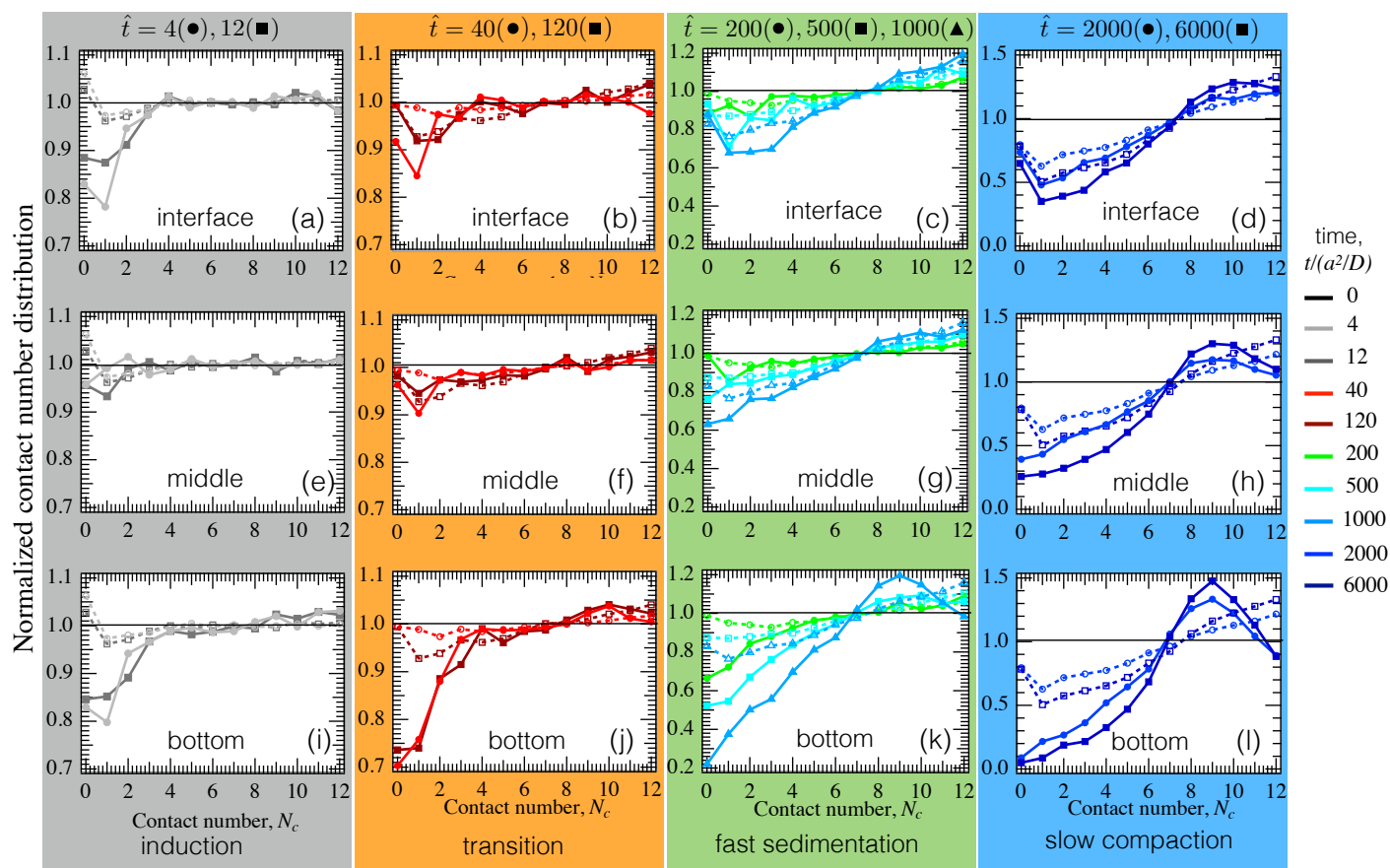


**Fig. 11** Normalized contact number distribution at several times for a  $5kT$  gel with particle weight  $Pe = 0.05$  for various spatial regions (filled symbols) and under quiescent conditions for the entire gel (open symbols). Rows from top to bottom indicate spatial regions: top of gel  $0.9 \leq z/h_{gel} \leq 1$ , middle of gel  $0.4 \leq z/h_{gel} \leq 0.8$ , and bottom of gel  $0.1 \leq z/h_{gel} \leq 0.2$ . Columns indicate various temporal regimes: Induction period ( $0 \leq \hat{t} \leq 12$ ) in gray, transition regime ( $12 \leq \hat{t} \leq 120$ ) in orange, fast sedimentation ( $120 \leq \hat{t} \leq 1200$ ) in green, and slow compaction ( $1200 \leq \hat{t} \leq 6000$ ) in blue.

We identify two distinct temporal regimes in the middle region:  $0 \leq \hat{t} \leq 500$  (no net densification), and  $\hat{t} \geq 1000$ , when the gel begins to densify. Plots (e) and (f) show that coarsening is no faster under gravity throughout induction until peak sedimentation, but later during rapid sedimentation, plot (g) reveals some enhanced coarsening where normalized contact number distribution reveals a more rapid migration of particles compared to a quiescent gel. Recalling that volume fraction is still temporally constant during this time in the middle region, we infer that  $P(N_c)$  shifts higher owing to coarsening migration rather than affine displacements. This acceleration of coarsening migration rather than a slow progression toward arrest supports the idea that the gel is phase separating and decreasing its potential energy during free-fall rather than simple coarsening.

Later, when densification of the middle layers commences (plot (h)), a decrease in the  $P(N_c) \leq 6$  and  $P(N_c = 11, 12)$  populations and an increase in populations of  $N_c = 9$  emerge, the latter in contrast to quiescent coarsening. That is, particles migrate away from the highest contact number populations to lower contact number populations under densification, which can only occur if pores in the gel have shrunk substantially. It is more favorable energetically for the volume in the pores to be subsumed by the strand surrounding the pore, providing additional free volume to

the condensed phase, allowing compressed bonds to relax and, in consequence, decrease in  $\langle PE \rangle$ .

Clearly affine flux plays a substantial role in densification and pore shrinkage in the bottom region at long times, but an additional contribution to particle flux may arise from the advection of phase separation: the motion of particles driven by activated release from kinetic arrest. This advection was suggested in Section 4.1.3 by the substantially higher sedimentation velocity of the gel in comparison to a suspension. The only driving force available to produce enhanced sedimentation velocity is from particle-phase osmotic pressure, which, if negative, drives the gel to condense (collapse) after the emergence of a free surface. That is, densification is not the result of affine bulk descent, but rather it is the cause: the gel is collapsing in on itself, i.e. phase separating. This precedes and drives macroscopic sedimentation, or collapse.

In summary, quantitative analysis of bond dynamics reinforces the idea that the tipping point is accompanied by small bond loss that drives an instability in the gel, triggering a cascade of changes arising from enhanced coarsening migration of particles from low to high contacts (and conversely, from high to low energy) — vertical pore growth that in turn leads to strand dissolution and creation of a rough surface, eventually leading to

ceiling detachment and smoothening the rough surface over several hundred Brownian times. In the bulk of the gel, gravity-enhanced coarsening precedes and drives densification, suggesting that densification arises not only due to particle advection toward the impermeable floor, but more importantly, due to non-equilibrium phase separation driven by interparticle attractions that lowers the average potential energy. The difference between compaction (the former mechanism) and collapse (the latter mechanism) can be distinguished even more clearly by measurements of osmotic pressure, discussed in the next section. Perhaps surprisingly, hydrodynamic interactions are not a necessary trigger or cause of gel collapse.

#### 4.4 Rheology: Osmotic Pressure

Thus far, we have identified that three distinct processes accompany collapse: enhanced coarsening migration, phase separation, and affine compaction. The challenge is to distinguish between affine compaction and phase separation during macroscopic descent; both result in bulk densification and pore shrinkage. The osmotic pressure can unambiguously differentiate the two processes.

Hallmarks of a release from kinetic arrest and post-gelation phase separation include negative osmotic pressure that drives an increase in volume fraction from pore shrinkage and the loss of surface area as the bi-continuous network becomes a bulk attractive glass (with a more sharply peaked distribution of contact number, few particles of  $N_c \leq 4$ , and a decrease in populations  $N_c \geq 10$  as particles fill in pores). While affine compaction should also increase volume fraction, drive pore shrinkage, and shift the contact number distribution, affine displacements push many particles toward hard-sphere contact, causing a shift toward *positive* osmotic pressure. Thus the evolution of osmotic pressure becomes the rheological characteristic that differentiates between when affine particle motion compacts the gel, and when internal osmotic pressure-driven phase separation collapses the gel from within.

The effect of particles and their interactions on osmotic pressure has been defined mechanically as the particle contributions to the negative of the trace of the equilibrium stress tensor<sup>45,48,49</sup> defined in Section 3,

$$\frac{\Pi}{nkT} = -\frac{1}{3} \frac{\mathbf{I} : \langle \boldsymbol{\Sigma} \rangle}{nkT} = 1 + \frac{\Pi^P}{nkT} + \dots, \quad (13)$$

where the first term on the right hand side is the ideal osmotic pressure and is always positive: diffusion tends to expand system boundaries.<sup>45</sup> The pair contribution  $\Pi^P$  can raise or lower osmotic pressure. A positive pair contribution to osmotic pressure also tends to expand a system outward, while condensing systems display  $\Pi^P < 0$ .<sup>8,45</sup> Only the elastic stress  $n\langle \mathbf{x}\mathbf{F}^P \rangle$  matters in a freely draining system, where hard-sphere repulsion (entropic exclusion) gives a positive osmotic pressure, and attractions give a negative contribution:

$$\frac{\Pi^P}{nkT} = \frac{\langle \mathbf{r} \cdot \mathbf{F} \rangle}{3kT}, \quad (14)$$

where  $\mathbf{r} \equiv \mathbf{X}_i - \mathbf{X}_j$  is the separation between a pair of particles

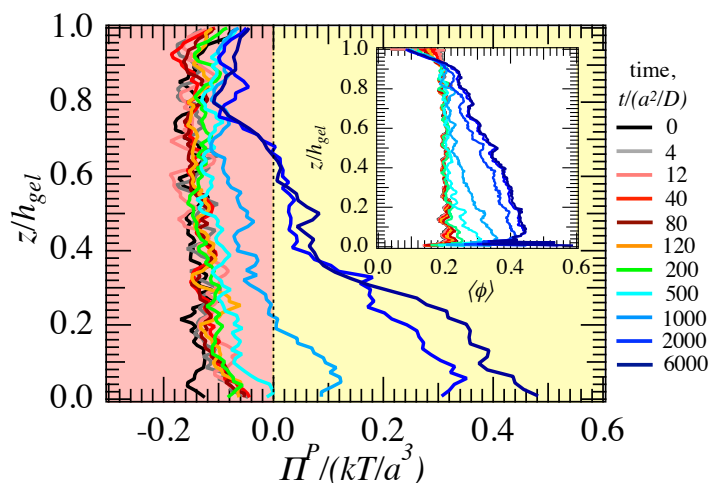


**Fig. 12** Osmotic pressure at depth of the gel for  $Pe = 0.05$ ,  $V_0 = 5kT$  at various times. The red shaded region indicates negative contribution to osmotic pressure, indicating many attractions, while the yellow region indicates positive contribution to osmotic pressure, indicating many repulsions. Inset shows corresponding layer-by-layer volume fraction.

$i$  and  $j$  at positions  $\mathbf{X}_i$  and  $\mathbf{X}_j$  respectively, and  $\mathbf{F}$  is the force derivable from the interparticle potential (cf Equation 1) for that separation. The angle brackets denote a sum over all pairs of interactions, divided by the number of particles. If the range of depletion attraction is smaller than a critical value,  $\Delta_{crit} \simeq 0.15$ , terms of order higher than  $O(n^2)$  may be neglected since three-particle overlaps are prohibited due to steric hindrance (see Section 5 in Supplementary Materials). The range of interparticle attraction for the gel studied in this work is  $\Delta = 0.1 < \Delta_{crit}$ .

When the interparticle force between the particles is repulsive,  $\mathbf{r} \cdot \mathbf{F} > 0$ , bonds are compressed and act to expand the particle phase, and  $\Pi^P > 0$ . When the interparticle force between the particles is attractive, negative osmotic pressure pulls particles together. This condensation tends to drive phase separation. Figure 2a illustrates that attractions arise when bonds are stretched,  $0 < s \leq 1$ . Physically, osmotic pressure is positive when particles can diffuse, either unhindered by attraction or when bonds are compressed, driving expansion of the particle phase. In contrast, osmotic pressure is negative in the presence of attractions when bonds are stretched, hindering diffusion and driving condensation. Although the gel is out of equilibrium, a decrease in potential energy decreases the Helmholtz free energy, consistent with phase separation.

We return to the interrogation of osmotic pressure in the gel arising from interparticle forces. Since the collapsing gel densifies over time (cf Figure 3b), we begin by plotting the layer-by-layer pair contribution to osmotic pressure for the falling gel in Figure 12 for several instants in time. For reference, the volume fraction variation with depth in the gel is shown in the inset.

Initially at  $\hat{t} = 0$ , the pair contribution to osmotic pressure is negative everywhere in the gel; in a quiescent gel this evolves slowly because attractive bonds want to relax but held out of their wells due to glassy frustration. During the induction period  $0 < \hat{t} \leq 12$ , recall that the gel sediments slowly with small changes in bulk height (cf Figure 5a), little change in volume fraction (cf

inset, Figure 12, and contact number and potential energy exhibit small fluctuations (cf Figure 10). Correspondingly, the pair contribution to osmotic pressure remains negative everywhere, exhibiting weak fluctuations relative to the initial value at  $\hat{t} = 0$ .

During the transition regime ( $12 \leq \hat{t} \leq 120$ ), some densification near the bottom is apparent in the inset, while a change in average contact number and average potential energy is detectable everywhere in the gel (Figure 10b). The pair contribution to osmotic pressure for every instant shown is now averaged over ten Brownian times. This reveals increased (less negative) osmotic pressure near the bottom of the gel ( $0 \leq z/h_{gel} \leq 0.1$ ) that is larger than the magnitude of fluctuations. However, most of these bonds are still stretched and the pair contribution to osmotic pressure is still negative, suggesting that the gel is condensing everywhere.

During rapid sedimentation  $120 < \hat{t} \leq 2000$ , the gel undergoes significant densification (inset in Figure 12), a rough interface of several pore sizes is apparent near the top of the gel (cf Figure 7), and average contact number increases while average potential energy decreases everywhere in the gel (cf Figure 10). Correspondingly, pairwise contribution to osmotic pressure (now averaged over 20 Brownian times), exhibits significant changes. The top of the gel ( $0.9 \leq z/h_{gel} \leq 1$ ) exhibits negative osmotic pressure, consistent with the picture of coarsening that drives the smoothing of the rough interface. Recall that the middle region in the gel ( $0.4 \leq z/h_{gel} \leq 0.8$ ) initially reveals no densification ( $t \leq 500$ ) but later undergoes an increase in volume fraction ( $t > 500$ ). Correspondingly, the pair contribution to osmotic pressure is negative in this region, suggesting that attractions dominate and drive phase separation, evidenced by both densification in this layer, and a decrease in potential energy ( $\langle PE \rangle / \langle PE_0 \rangle > 1$ ), consistent with the picture of release from kinetic arrest. The bottom of the gel ( $0.1 \leq z/h_{gel} \leq 0.2$ ) is also densifying but the corresponding pair contribution to osmotic pressure is positive, indicative of repulsive interactions between particles arising from bond compression that dominate when affine compaction pushes particles closer to each other after phase separation has first relaxed bonds and collapsed the gel, releasing it downward. Overall, this supports the idea that gravity-enhanced migration triggers an instability in network strand structure that permits release from kinetic arrest, all driven by osmotic pressure gradients.

Finally during the late-stage slow compaction regime, when the sedimentation rate decays rapidly (cf Figure 7), and height changes are small (cf Figure 5a), the pair contribution to osmotic pressure is predominantly positive in the bulk of the gel, except below and at the interface between the gel and the supernatant, where osmotic pressure is negative for  $0.7 \leq z/h_{gel} \leq 1$ . This suggests that the interface continues to coarsen to reduce surface area and, beneath it, ongoing condensation allows the gel to further densify.

Only at very long times does the osmotic pressure become mostly positive; when  $\Pi^P > 0$  in over 70% of the collapsed gel, the gel seems to re-arrest, i.e. sedimentation slows but bi-continuous structure remains. This re-arrest occurs evidently because gravitational forcing pushes particles toward one another, beyond the bond minimum, creating compressed bonds that produce a positive osmotic pressure; this in turn inhibits phase separation. Col-

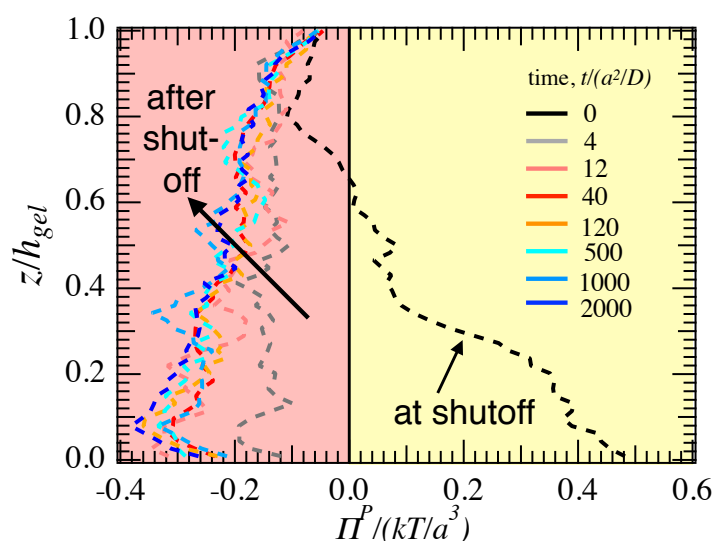


**Fig. 13** Osmotic pressure at depth of the gel  $V_0 = 5kT$  at various times after gravity is shut off after gel approaches the final height under  $Pe = 0.05$ . The red shaded region indicates negative contribution to osmotic pressure, indicating many attractions, while the yellow region indicates positive contribution to osmotic pressure, indicating many repulsions.

lapse evidently ends when the forcing due to phase separation, i.e. the negative osmotic pressure driving collapse, is resisted by positive osmotic pressure. That is, the gel collapses in on itself due to activated phase separation and somewhat counterintuitively, gravity causes re-arrest — compressed bonds and more jammed structure.

This hypothesis may be tested in simulation by turning off gravitational forcing after the gel reaches its final height, and monitoring the pair contribution to osmotic pressure and subsequent evolution of the gel. If gravity indeed acts to arrest ongoing phase separation by jamming the structure, “shutting off” gravity should produce negative osmotic pressure but little coarsening — i.e. a more deeply arrested gel. The layer-by-layer pair contribution to osmotic pressure is plotted in Figure 13 after shutting off gravity for several instants in time. Within four Brownian times, the osmotic pressure becomes negative everywhere in the gel, suggesting that many compressed bonds have now relaxed, and thus that gravity halted condensation by jamming particles together. Over time in the absence of gravity, the osmotic pressure deeper in the container becomes more negative, where volume fraction is higher (cf Figure 3a). This picture is consistent with the layer-by-layer analysis of bond dynamics (cf Figure 10a) which revealed that deeper layers in the gel have a higher mean contact number and thus particles have more bonds, which initially relax when gravity is removed, resulting in a more negative osmotic pressure. Evolution of contact number distribution after turning off gravity will reveal whether the negative osmotic pressure in the dense sediment results in further condensation of the gel or whether the dense sediment is jammed and further bond relaxation is hindered by steric hindrance.

If affine compaction did not re-arrest the gel, instead permitting phase separation to continue, the final morphology would approach that of a dense sediment devoid of pores, i.e., an attrac-

tive glass.

We compare the collapsing gel to an attractive glass prepared from a repulsive glass of volume fraction  $\phi = 0.62$ , where an attractive interparticle potential is imposed, as would occur by adding depletant to a repulsive glass in an experiment.<sup>42</sup> We compare the contact number distribution in the bottom layer in the gel to that of the attractive glass in Figure 14a. The two most important features of the data for the attractive glass are a sharp peak at  $N_c = 9$ , and a vanishingly small population for  $N_c \leq 4$  that, combined, confirm that it is devoid of pores of more than a particle size, and is devoid of surface particles. In contrast, the bi-continuous gel initially exhibits a broad distribution where extensive surface area permits a significant population size for  $N_c \leq 4$ . During collapse ( $0 \leq t \leq 6000$ ), the distribution in the gel moves toward the right and is more sharply peaked as pores shrink, and moves toward the distribution of the attractive glass, but never completely so, evidently prevented by re-arrest due to gravity. Remarkably, after gravitational forcing is removed, Figure 14a reveals that the change in contact number distribution is barely discernible even after 2000 Brownian times, suggesting that further condensation is very slow, despite the negative osmotic pressure seen in Figure 13b. This suggests that glassy frustration is too deep (particle mobility is low).

That is, it appears that the requirement for condensation is not only a negative osmotic pressure, but also that the particles with negative osmotic pressure are mobile enough to drive bond relaxation.

A more refined predictor of collapse is the partial pressure exerted by each population that can reveal whether mobile, surface particles or deeply embedded particles contribute to the negative osmotic pressure; in the former, negative osmotic pressure would drive collapse, in the latter, jamming will prevent phase separation. The partial pressure of each  $N_c$  population (the per-particle pressure weighted by its population size), is normalized on  $nkT$  and plotted as a function of  $N_c$  in Figure 14b. The primary features of the partial pressure in the attractive glass are a zero pressure for  $N_c \leq 4$ , and sharply negative values for  $7 \leq N_c \leq 11$ . The single-phase domain with no surface area (the attractive glass) drives the former effect. The latter effect evidences deep glassy frustration, where bonds are pulled out of their wells and held stretched by jammed morphology. In contrast, in the gel, the partial pressure for the bottom layer is *initially* negative for all  $N_c \leq 10$  with a negative minimum at  $N_c = 6$ ; that is, highly mobile populations have a negative osmotic pressure. During collapse, it is the negative partial pressure of mobile particles (data for the middle layer of the gel shown in Figure S8 in Supplementary Materials) that drives condensation, and densification of the gel.

Eventually, affine compaction pushes particles toward one another, and the partial pressure becomes positive for  $N_c \geq 7$  by  $\hat{t} = 6000$ . By shutting off gravity, these compressed bonds relax and partial pressure becomes once again negative for all populations, also evident from bond-length distribution, shown in Figure S10 in Supplementary Materials. However, the partial pressure now exhibits a negative peak at  $N_c = 9$  after removal of gravity, differing significantly from the initial gel, and revealing similarities to the attractive glass for  $N_c \geq 9$ , suggesting re-arrest of the

gel.

Overall, several signals combine to suggest that collapse is gravity-triggered phase separation driven by osmotic pressure: a sedimentation rate much faster than that of a dispersion; densification with overall negative osmotic pressure; and decreasing potential energy. Collapse eventually permits bond compression due to direct gravitational compaction that drives positive osmotic pressure causing re-arrest of the gel. This re-arrest prevents further condensation of the gel and is evident after removing gravity: more negative partial pressures corresponding to sterically hindered particles that cannot relax.

The pair contribution to osmotic pressure, averaged over the entire gel is plotted in Figure 15 during collapse. The pressure is initially negative with little discernible change during the induction period ( $0 \leq \hat{t} \leq 12$ ). During the transition period ( $12 \leq \hat{t} \leq 120$ ), the pressure increases (becomes less negative) and continues growing through fast sedimentation. The pressure becomes positive at  $\hat{t} \approx 1400$  late into the rapid sedimentation regime. In the inset, the sedimentation rate is shown for the same gel. When pressure becomes positive, the sedimentation rate has decreased to less than half its peak value, and the transition to late-stage slow compaction occurs. Overall, it appears that collapse stops when condensation stops. In other words, when gravitational forcing drives particles away from the energy minima compressing bonds leading to an overall positive pair contribution to osmotic pressure, it inhibits phase separation, and causes the gel to re-arrest.

## 5 Conclusions

A freely draining, reversible gel successfully captures the three temporal regimes of gel collapse — a slow induction period, followed by rapid sedimentation, and final slow compaction. This behavior has been extensively studied<sup>15–23,25–28,50</sup> and is found to be exhibited by gels ranging from permanently bonded fractal networks to loose aggregates. While macroscopic behavior is easily tracked, understanding of the structural changes that occur during collapse have proven difficult to measure in experiments. In the present study, the large-scale computational model provides access to detailed information about particle positions and structure to examine collapse and gain insights into its microstructural origins. We modeled a freely-draining system comprising 750,000 particles interacting via a hard-sphere repulsion and short-range attraction potential several times stronger than the thermal energy,  $kT$ . The interplay between attractive forces and Brownian motion initiates a phase separation that arrests before it is complete,<sup>3,4</sup> freezing in a bi-continuous, non-equilibrium morphology with thick, non-fractal strands that continue to restructure and coarsen over time. Gelation and aging were carried out in the absence of gravity, i.e. on neutrally buoyant particles. A body force corresponding to gravity was then applied, and varied to mimic a range of particle densities relative to the solvent. A hard “floor” and “ceiling” gave no-flux and no-slip interfaces that were modeled as sticky or repulsive. The purpose of the present computational study was to recover and study the collapse behavior over all its temporal regimes, to understand the structural origins of the “tipping point” between slow induction

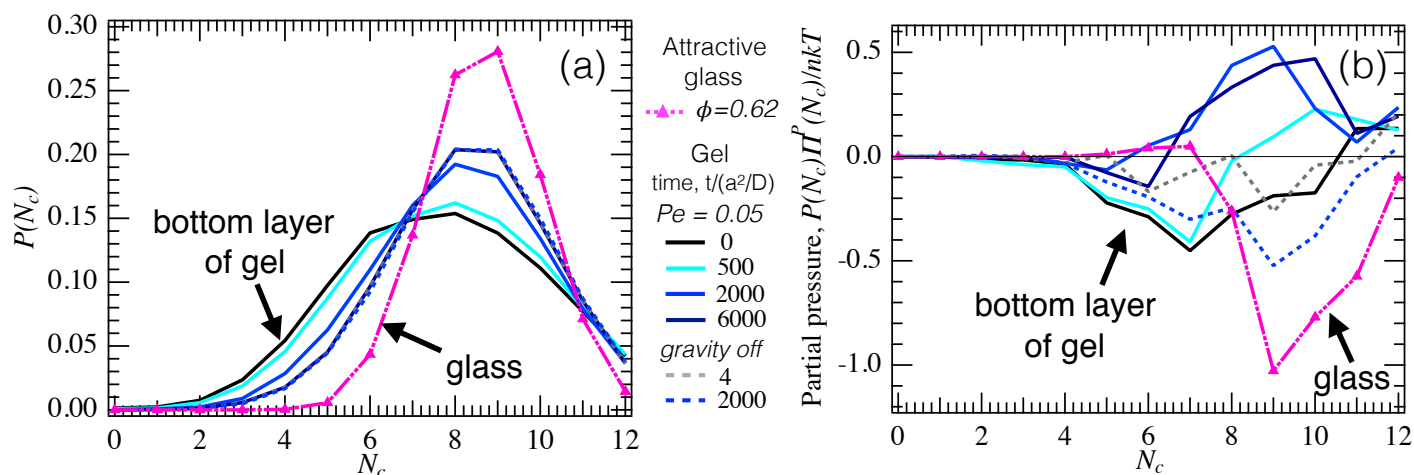


**Fig. 14** Comparison between an attractive glass and the bottom layer of the gel ( $0.1 \leq z/h_{gel} \leq 0.2$ ) with bond strength  $V_0 = 5kT$  during collapse and after shutting off gravity. (a) Contact-number distribution,  $P(N_c)$ , and (b) partial pressure, normalized on  $nkT$ .

and fast collapse, and to identify the driving force of gel collapse.

Macroscopic analysis of sedimentation behavior showed that even this simple model of a freely draining gel recovers the three distinct macroscopic hallmarks of gel collapse — a slow induction period that ends in a tipping point, followed by a transition to rapid sedimentation, and a final, slow compaction regime, are recovered. Comparison to settling of a freely draining hard-sphere dispersion showed that delayed yield requires durable interactions (i.e. bonds) but not hydrodynamic interactions. Surprisingly, gel collapse is faster than sedimentation of a freely draining suspension of purely repulsive hard spheres, a result of the additional driving force of negative osmotic pressure acting to condense the particle phase. The driving force grows stronger with stronger bonds: a mechanically “stronger” gel collapses faster, owing to the depth of its position beneath the spinodal. Overall this suggests that a non-equilibrium phase separation, triggered by gravity-induced particle migration and growing from a capillary-like instability, is the central process underlying collapse.

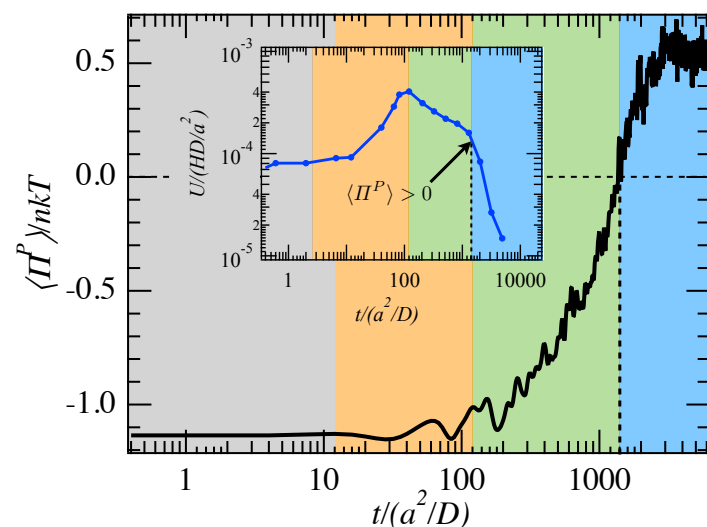


**Fig. 15** Pair contribution to osmotic pressure versus time for the collapsing gel with bond strength  $V_0 = 5kT$  and particle weight  $Pe = 0.05$ . Inset shows the sedimentation rate for the same gel.

Structural analysis revealed the surprising result that collapse can occur with a fully intact, space-spanning network. The tipping point from slow compaction to collapse evidently arises from unstable particle migration that produces a capillary-like instability, where particles migrate away from the length of a strand toward a junction. Owing to the strong influence of Brownian motion, this growing instability manifests as a transition from pore widening to rapid vertical pore growth accompanied by a minor loss in bonds. When hydrodynamic interactions play a role, they are the “caboose”, whereas triggered phase separation is the “engine”.

The idea that densification is caused by phase separation is further confirmed via measurements of osmotic pressure. Interparticle attractions produce a negative osmotic pressure in the middle layers of the gel that drive its condensation, causing gel collapse as stretched bonds relax. But, comparison to an attractive glass reveals that a negative osmotic pressure alone is not sufficient to drive collapse if particles are jammed and cannot restructure owing to steric hindrance. Instead, rapid collapse requires

both appreciable particle mobility and negative osmotic pressure, which together permit bond relaxation. Concomitant measurements of the potential energy are consistent with the idea that a spontaneous process is taking place whereby the gel lowers its energy by condensing — where the final volume fraction places the final “phase” well to the right of the binodal. That is, a non-equilibrium phase separation process permitted a leap to the right in the phase diagram and downward to a lower energy state. At long times, gravity compresses bonds, driving a positive value of osmotic pressure, coinciding with a rapid decay in sedimentation rate. Thus, collapse stops when condensation stops.

Counterintuitively, the role of gravity is to activate the release from kinetic arrest allowing condensation and phase separation to proceed, and subsequently compress some bonds causing the gel to re-arrest and prevent complete phase separation.

We emphasize that this model is valid for reversibly bonded gels formed via arrested phase separation. Other gels formed from purely kinetic and non-thermodynamic routes such as DLCA or jamming,<sup>3,4</sup> and patchy colloids where the phase diagrams<sup>51</sup> differ significantly from Figure 1, may behave differently.

The view that collapse offers a non-equilibrium route of traversing (tunneling) through the energy landscape from one arrested state to another arrested state poses interesting questions about how we should view so-called arrested states of matter. We propose that such non-equilibrium routes out of the equilibrium phase diagram can be viewed as “phase mechanics”, a combination of behaviors that characterize colloidal gel responsiveness: thermodynamic, kinetic, and mechanical phase transition. Such a view may provide further insight into the design of engineered materials, as well as deeper understanding of phase transitions that accompany highly non-equilibrium processes, such as those observed inside eukaryotic cells during division, for example.

## Acknowledgements

The authors wish to acknowledge many helpful conversations with Dr. Benjamin J. Landrum, Lilian C. Johnson, and J. Galen Wang. This work was supported by NSF CAREER Grant (CBET-1351184), an Office of Naval Research Young Investigator Award (N00014-14-1-0744), and the National Science Foundation Extreme Science and Engineering Discovery Environment (XSEDE) Research Award No. OCI-1053575, utilizing the TACC and Stampede computational resource.

## Appendix A: Height Detection Algorithm

Measurement of bulk gel height as it evolves (descends) over time, the primary metric of gel collapse, requires identification of an interface between the bulk gel and the emerging supernatant fluid. Experimental measurements of evolving gel height have been obtained via dark-field images<sup>17</sup>, suggesting a volume-fraction criterion for identification of the interface. Precise identification of an interface can prove challenging, owing to the colloidal-scale and network pore-scale bumpiness of a newly detached surface. In contrast, in molecular systems, such interfaces are molecularly smooth; the “volume fraction” at the interface,  $\phi_{int}$ , is sharply defined as  $\phi_{int} = (\phi_{liquid} - \phi_{gas})/2$ . For a colloidal gel, a naive approach would be employ a similar criterion:

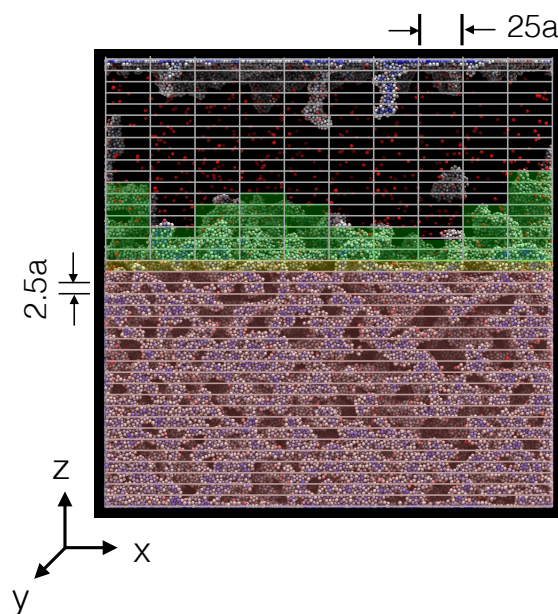


**Fig. A1** (a) Schematic to calculate the cells used to calculate instantaneous height of the gel from particle positions. Lines and shaded regions depict the algorithm to calculate average gel height. Red layers have  $\langle \phi \rangle(z) > \phi_{cutoff}$ , yellow is the lowest layer with  $\langle \phi \rangle(z) \leq \phi_{cutoff}$ . Region above the yellow layer are divided into cells. Green cells have  $\langle \phi \rangle(x, y, z) > \phi_{int}$  and designated to belong to the gel, while unshaded dark cells depict regions possess  $\langle \phi \rangle(z) < \phi_{int}$  and are thereby assigned supernatant.

$\phi_{int} = (\phi_{gel} - \phi_{supernatant})/2$ . The supernatant has few colloidal particles, and thus  $\phi_{supernatant} \rightarrow 0$ . However, several complications arise. First, while the average volume fraction of the gel prior to deformation is uniform over lengths of several pore sizes, compaction is likely to produce a spatially dependent volume fraction,  $\phi_{gel}(z)$ . To resolve this ambiguity, one might assume that the gel near the detaching interface retains the original volume fraction, and set  $\phi_{int} = \langle \phi_{gel} \rangle(t=0)/2$ . But even this definition is ambiguous: the local volume fraction within a gel varies over several particle length scales, and the gel itself contains colloid-poor voids<sup>8</sup>. This difficulty is most pronounced at the emerging interface, which is rough with exposed pores and dangling strands, as illustrated in Figure A1. Finally, bulk descent during the initial duration of collapse does not produce a container-wide supernatant, and resolution in only the  $z$ -direction is insufficient to capture the changes in height until a container-wide supernatant emerges.

We developed a height-detection algorithm that overcomes these issues. The simulation box is divided into a 100 horizontal layers ( $x$ - $y$  plane), each of thickness  $2.5a$ , stacked in the vertical ( $z$ ) direction. These layers are static, and do not change for the height calculation. The average volume fraction within each layer is computed as follows:

$$\langle \phi \rangle(z) = \frac{\sum_i 4\pi a_i^3 / 3}{V_{layer}}, \quad (15)$$

where the angle brackets denote an average over the layer centered at  $z$ , computed by adding the volume of every particle  $i$

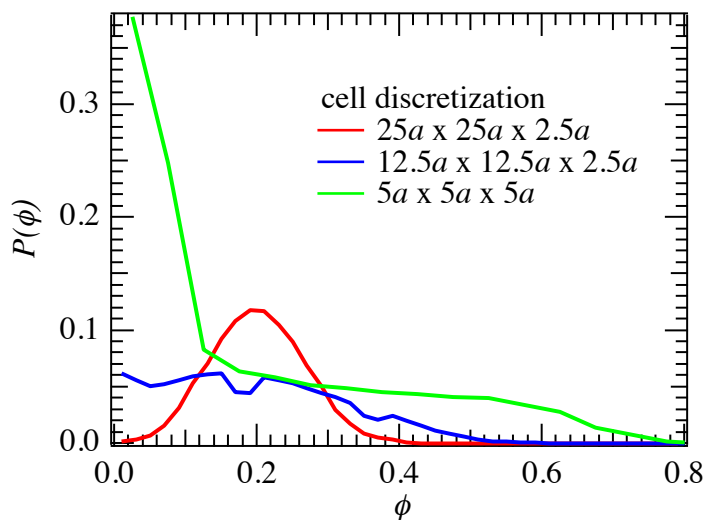


**Fig. A2** Distribution of volume fraction in a cell of various resolutions of discretization.

located in the layer divided by the volume of the cuboidal layer,  $V_{layer}$ .

$$V_{layer} = N/100n, \quad (16)$$

where  $N$  is the total number of particles in the container,  $n$  the initial number density, and  $N/n$  gives the volume of the container.

Average volume fraction in the horizontal layers are examined in the container, and are expected to decrease going from the bottom to the top, with an extended interface. The bottommost layer that has a lower average volume fraction than the threshold of  $\phi_{cutoff} = 0.75\langle\phi\rangle(t=0)$ , is used as an initial estimate of the location of the interface, illustrated as a shaded yellow layer in Figure A1. To account for roughness of the interface and dangling strands, the horizontal layers above the yellow layer are further divided in the  $x$  and  $y$  directions into cuboidal ‘‘cells’’. The idea is that the average volume fraction within the cell is used to estimate the ‘local’ height of the rough interface, and an average over all the local heights determines the average height of the gel. The aspect ratio of the cell must be sufficiently larger than a typical solvent pore size within the bi-continuous structure so that solvent pores within the gel are not mistaken as the interface, yet the aspect ratio must have sufficient resolution to yield an accurate average height of the gel. The average volume fraction within each cell is computed as:

$$\langle\phi\rangle(x,y,z) = \frac{\sum_i 4\pi a_i^3/3}{V_{cell}}, \quad (17)$$

where the angle brackets denote an average over the cell centered at  $(x,y,z)$ , computed by adding the volume of every particle  $i$  located in the cell divided by the volume,  $V_{cell}$ . The aspect ratio of the cell was determined by plotting (Figure A2) the distribution of average volume fraction in a quiescent gel for various cell sizes, as described by the legend. The discretization  $25a \times 25a \times 2.5a$  (red curve) was chosen because it produced a normal distribution about the average volume fraction of the initial colloidal gel, and supernatant, described by  $\langle\phi\rangle(x,y,z) \rightarrow 0$  would not be de-

tectable in a quiescent gel, whereas smaller cells (green and blue curves) would incorrectly ascribe solvent pores as belonging to the supernatant. The chosen discretization provides 100 cells in each horizontal layer above the yellow layer, distinguishable by indices  $i$  in the  $x$ -direction, and  $j$  in the  $y$ -direction.

Above the yellow layer, the height of the interface  $h_s(i,j)$ , is calculated for every vertical column of cells at  $(i,j)$ , as the vertical center of the bottommost cell where the volume fraction falls below  $\phi_{int}$ . In Figure A1, the shaded green cells have  $\langle\phi\rangle(x,y,z) > \phi_{int}$ , whereas the dark cells have  $\langle\phi\rangle(x,y,z) < \phi_{int}$ . An average over all vertical columns gives the instantaneous average height of the gel  $h_{gel}$ :

$$h_{gel} = \frac{\sum_{j=1}^{10} \sum_{i=1}^{10} h_s(i,j)}{100} \quad (18)$$

The height of the gel is computed from particle positions, at every instant of time, that permits calculation of sedimentation rate, measurement of pore cross-section near the container boundaries, and a time-dependent division of the gel into horizontal layers to interrogate layer-by-layer quantities such as contact number, potential energy, and osmotic pressure.

## Appendix B: Layer-by-layer averages within the gel

As the gel undergoes collapse, analysis of volume fraction reveals changes not only in time, but also within the gel; therefore, it is expected that bond dynamics and osmotic pressure correspondingly evolve in time and vary within the gel. To study this variation within the gel, average quantities are computed within horizontal slices (layers) in the gel at all instants in time.

For computation of the layer-by-layer average contact number, the contact number for each particle  $i$  at time  $t$ ,  $N_c(i,t)$  is computed as described in Section 4.3, by counting the number of nearest-neighbor bonds. The gel is then divided into horizontal slices of equal thickness. A particle belongs to a horizontal slice  $L$  if its center of mass lies within the slice. The average contact number within the slice  $L$  at time  $t$  (denoted by  $\langle N_c \rangle(t)$ ), is computed by summing over the contact number of all particles in the slice divided by the number of particles in the slice,

$$\langle N_c \rangle(t) = \frac{\sum_{i=1}^{N_L(t)} N_c(i,t)}{N_L(t)}. \quad (19)$$

Here,  $N_L(t)$  is the total number of particles within the layer  $L$  at time  $t$ . The quantity  $\langle N_c \rangle(t)$  is colorized by layer  $L$ , normalized on its initial value, and plotted in Figure 10a as a function of diffusively-scaled time.

To compute layer-by-layer average potential energy, one cannot directly use Equation 12 because potential energy  $V_{ij}(t)$  pertains to a bond, which can be formed by two particles in different horizontal slices, making the definition of potential energy within a layer ambiguous. Instead, one can define the potential energy of a particle  $i$  at time  $t$ ,  $V_i(t)$ , as half the sum over the energy of all bonds with nearest neighbors. Subsequent computation of layer-by-layer average potential energy is similar to that of average contact number. The gel is divided into horizontal slices

of equal thickness, and the average within the slice (denoted by  $\langle PE \rangle(t)$ ) is computed by summing over the potential energy of all particles in the slice divided by the number of particles in the slice,

$$\langle PE \rangle(t) = \frac{\sum_{i=1}^{N_L(t)} V_i(t)}{N_L(t)}. \quad (20)$$

Here,  $N_L(t)$  is the total number of particles within the layer  $L$  at time  $t$ . The quantity  $\langle PE \rangle(t)$  is colorized by layer  $L$ , normalized on its initial value, and plotted in Figure 10b as a function of diffusively-scaled time.

The layer-by-layer osmotic pressure is computed from the layer-by-layer average of  $\mathbf{r} \cdot \mathbf{F}$  using Equation 14, where  $\mathbf{r}$  is the distance between particles in a bonded pair and  $\mathbf{F}$  is the force due to the interaction. Similar to the potential energy per particle, an unambiguous layer-by-layer quantity requires computation of  $\mathbf{r} \cdot \mathbf{F}$  for every particle  $i$ , by summing over half the contribution of  $\mathbf{r} \cdot \mathbf{F}$  from all bonds with nearest neighbors. The layer-by-layer average is then computed by summing over all particles within the layer and dividing by the total number of particles within the layer. Layer-by-layer osmotic pressure is then computed using Equation 14.

## References

- 1 B. J. Landrum, W. B. Russel and R. N. Zia, *Journal of Rheology*, 2016, **60**, 783–807.
- 2 V. J. Anderson and H. N. W. Lekkerkerker, *Nature*, 2002, **416**, 811–815.
- 3 E. Zaccarelli, *Journal of Physics: Condensed Matter*, 2007, **19**, 323101.
- 4 P. J. Lu, E. Zaccarelli, F. Ciulla, A. B. Schofield, F. Sciortino and D. A. Weitz, *Nature*, 2008, **453**, 499–503.
- 5 N. A. M. Verhaegh, D. Asnaghi, H. N. W. Lekkerkerker, M. Giglio and L. Cipelletti, *Physica A*, 1997, **242**, year.
- 6 H. Tanaka, *Journal of Physics: Condensed Matter*, 2000, **12**, R207.
- 7 W. C. K. Poon, *Journal of Physics: Condensed Matter*, 2002, **14**, R859.
- 8 R. N. Zia, B. J. Landrum and W. B. Russel, *Journal of Rheology*, 2014, **58**, 1121–1157.
- 9 L. C. Johnson and R. N. Zia, *under preparation*.
- 10 L. C. Johnson, B. J. Landrum and R. N. Zia, *under preparation*.
- 11 V. Kobelev and K. S. Schweizer, *Journal of Chemical Physics*, 2005, **123**, 164902.
- 12 J. Kim, D. Merger, M. Wilhelm and M. Helgeson, *Journal of Rheology*, 2015, **58**, 1359–1390.
- 13 J. D. Park, K. H. Ahn and N. J. Wagner, *Journal of Rheology*, 2017, **61**, 117–137.
- 14 E. Moghimi, A. R. Jacob, N. Koumakis and G. Petekidis, *Soft Matter*, 2017, **13**, 2371–2383.
- 15 S. J. Partridge, *PhD thesis*, Bristol University, 1985.
- 16 C. Allain, M. Cloitre and M. Wafra, *Physical Review Letters*, 1995, **73**, 1478–1481.
- 17 W. C. K. Poon, L. Starrs, S. P. Meeker, A. Moussaïd, R. M. L. Evans, P. N. Pusey and M. M. Robins, *Faraday Discussions*, 1999, **112**, 143–154.
- 18 L. Starrs, W. C. K. Poon, D. J. Hibberd and M. M. Robins, *Journal of Physics: Condensed Matter*, 2002, **14**, 2485–2505.
- 19 M. L. Kilfoil, E. E. Pashovski, J. A. Masters and D. A. Weitz, *Philosophical Transactions of the Royal Society A*, 2003, **361**, 753–766.
- 20 S. Manley, J. M. Skotheim, L. Mahadevan and D. A. Weitz, *Physical Review Letters*, 2005, **94**, 218302.
- 21 V. Gopalakrishnan, K. S. Schweizer and C. F. Zukoski, *Journal of Physics: Condensed Matter*, 2006, **18**, 11531–11550.
- 22 S. W. Kamp and M. L. Kilfoil, *Soft Matter*, 2009, **5**, 2438.
- 23 C. Kim, Y. Liu, A. Kühnle, S. Hess, S. Viereck, T. Danner, L. Mahadevan and D. A. Weitz, *Physical Review Letters*, 2007, **99**, 028303.
- 24 J. J. Liétor-Santos, C. Kim, P. J. Lu, A. Fernández-Nieves and D. A. Weitz, *The European Physical Journal E*, 2009, **28**, 159–164.
- 25 L. J. Teece, M. A. Faers and P. Bartlett, *Soft Matter*, 2011, **7**, 1341–1351.
- 26 P. Bartlett, L. J. Teece and M. A. Faers, *Physical Review E*, 2012, **85**, 021404.
- 27 R. Harich, T. W. Blythe, M. Hermes, E. Zaccarelli, A. J. Sederman, L. F. Gladden and W. C. K. Poon, *Soft Matter*, 2016, **12**, 4300–4308.
- 28 E. Secchi, S. Buzzaccaro and R. Piazza, *Soft Matter*, 2014, **10**, 5296 – 5310.
- 29 H. N. W. Lekkerkerker and R. Tuinier, *Colloids and the depletion interaction*, Springer Netherlands, 2011.
- 30 R. M. L. Evans and L. Starrs, *Journal of Physics: Condensed Matter*, 2002, **14**, 2507–2529.
- 31 M. A. Faers, *Advances in Colloid and Interface Science*, 2003, **106**, 23–54.
- 32 R. Buscall and L. R. White, *Journal of the Chemical Society, Faraday Transactions 1*, 1987, **83**, 873–891.
- 33 W. B. Russel, D. A. Saville and W. R. Schowalter, *Colloidal Dispersions*, Cambridge University Press, 1989.
- 34 G. Brambilla, S. Buzzaccaro, R. Piazza, L. Berthier and L. Cipelletti, *Physical Review Letters*, 2011, **99**, year.
- 35 S. Buzzaccaro, E. Secchi, G. Brambilla, R. Piazza and L. Cipelletti, *Journal of Physics: Condensed Matter*, 2012, **24**, year.
- 36 M. Laurati, G. Petekidis, N. Koumakis, A. B. Schofield, J. Brader, M. Fuchs and S. U. Egelhaaf, *The Journal of Chemical Physics*, 2009, **130**, 134907.
- 37 M. E. Helgeson, S. E. Moran, H. Z. An and P. S. Doyle, *Nature Materials*, 2012, **11**, 344–352.
- 38 S. J. Plimpton, *Journal of Computational Physics*, 1995, **117**, 1–19.
- 39 G. K. Batchelor, *Journal of Fluid Mechanics*, 1970, **41**, 545–570.
- 40 G. K. Batchelor, *Journal of Fluid Mechanics*, 1977, **83**, 97–117.
- 41 K. N. Pham, A. M. Puertas, J. Bergenholtz, S. U. Egelhaaf, A. Moussaïd, P. N. Pusey, A. B. Schofield, M. E. Cates, M. Fuchs and W. C. K. Poon, *Science*, 2002, **296**, 104 – 106.
- 42 K. N. Pham, S. U. Egelhaaf, P. N. Pusey and W. C. K. Poon,

- Physical Review E*, 2004, **69**, 011503.
- 43 K. N. Pham, G. Petekidis, D. Vlassopoulos, S. U. Egelhaaf, W. C. K. Poon and P. N. Pusey, *Journal of Rheology*, 2008, **52**, 649–676.
- 44 R. Buscall, T. H. Choudhury, M. A. Faers, J. W. Goodwin, P. A. Luckham and S. J. Partridge, *Soft Matter*, 2009, **5**, 1345–1349.
- 45 R. N. Zia and J. F. Brady, *Journal of Rheology*, 2012, **56**, 1175–1208.
- 46 M. Bouzid, J. Colombo, L. V. Barbosa and E. D. Gado, *Nature Communications*, 2017, **8**, 15846.
- 47 W. C. K. Poon, *Science*, 2004, **304**, 830–831.
- 48 J. F. Brady, *Journal of Chemical Physics*, 1993, **4**, 3335.
- 49 H. C. W. Chu and R. N. Zia, *Journal of Rheology*, 2016, **60**, 755.
- 50 G. G. Glasrud, R. C. Navarette, L. E. Scriven and C. W. Macosko, *AIChE Journal*, 1993, **39**, 560–568.
- 51 E. Bianchi, J. Largo, P. Tartaglia, E. Zaccarelli and F. Sciortino, *Physical Review Letters*, 2006, **97**, year.